Electronic Supplementary Material (ESI) for Chemical Science.
This journal is © The Royal Society of Chemistry 2023

Supporting information for

Maximized axial helicity in a Pd_2L_4 cage: inverse guest size-dependent compression and mesocate isomerism

Witold M. Bloch,*[ab] Shinnosuke Horiuchi,[ac] Julian J. Holstein,[a] Axel Wuttke,[d] Wolf Hiller,[a] Ricardo A. Mata,[d] and Guido H. Clever*[a]

[a]*Department of Chemistry and Chemical Biology, TU Dortmund University, Otto-Hahn-Straße 6, 44227 Dortmund (Germany).*

[b]*Institute for Nanoscale Science and Technology, College of Science and Engineering, Flinders University, Adelaide, South Australia 5042, Australia*

[c]*Division of Chemistry and Materials Science, Graduate School of Engineering, Nagasaki University, Bunkyo-machi, Nagasaki, 852-8521 (Japan).*

[d]*Institute for Physical Chemistry, Georg-August University Göttingen, Tammannstraße 6, 37077 Göttingen (Germany*).

Contents

1. Experimental Section

1.1. Materials and measurements

Unless otherwise stated, all chemicals were obtained from commercial sources and used as received. Compounds **1** and **2** were prepared according to literature procedures.[1,2,3] $[Pd(CH_3CN)_4](ClO_4)_2$, $[Pd(CH_3CN)_4](PF_6)_2$, $[Pd(CH_3CN)_4](SbF_6)_2$, $[Pd(CH_3CN)_4](OTf)_2$ and $[Pd(CH_3CN)_4](NTf)_2$ were prepared in situ by reacting $Pd(CH_3CN)_2Cl_2$ with the respective silver salt in a 1:2 ratio. The AgCl precipitate was separated from the solution by centrifugation. Infrared spectra (IR) were collected on a Pelkin Elmer Spectrum Two spectrometer. Electrospray ionization (ESI) mass spectra were recorded on a Bruker Apex IV ESI-FTICR Mass Spectrometer with a dual electrospray ionization source. Ion-Mobility mass spectrometry was carried out with a Bruker timsTOF instrument. GPC purification of ligand **L** was performed on a JASCO LC-9210 II NEXT apparatus. Isothermal Titration Calorimetry (ITC) measurements were performed on a Malvern MicroCal PEAQ-ITC instrument at 25 °C.

1.2. Synthesis of Ligand (L)

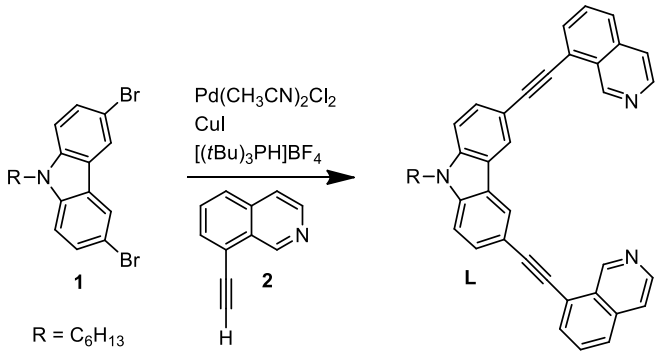

*1.2.1. Synthesis of 9-hexyl-3,6-bis(isoquinolin-8-ylethynyl)-9H-carbazole (**L**)*

Compound **1** (0.310, 0.758 mmol) and compound **2** (0.273 g, 1.78 mmol) were combined in a mixture of dioxane and triethylamine (3:1, 12 mL) in a Schlenk vessel. Once the solvent was degassed (via freeze-thaw cycles), $Pd(CH_3CN)_2Cl_2$ (0.012 g, 0.046 mmol), CuI (0.008 g, 0.042 mmol), and tri-*tert*-butylphosphonium tetrafluoroborate (0.024 g, 0.083 mmol) were added in one portion. The reaction mixture was subsequently heated at 80 °C for 16 h. Once allowed to cool, the mixture was diluted with ethyl acetate (20 mL) and the salts were removed by filtration. After concentrating under reduced pressure, the residue was purified by column chromatography (9:1 dichloromethane/methanol) followed by GPC to yield the title compound as a pale brown solid (0.212 g, 51 %). Mp 163.2 – 164.4 °C; ν_{max} (neat, cm^{-1}): 2924 (w), 2199 (m), 1612 (m), 1566 (s), 1484 (s), 1466 (m). ^{1}H NMR (500 MHz, $CDCl_3$) δ 9.95 (s, 2H, H_i), 8.63 (s, 2H, H_h), 8.47 (d, *J* = 1.6 Hz, 2H, H_c), 7.88 (dd, *J* = 7.2, 1.1 Hz, 2H, H_d), 7.84 – 7.78 (m, 4H, H_b, H_f), 7.73 – 7.66 (m, 4H, H_g, H_e), 7.47 (d, *J* = 8.5 Hz, 2H, H_a), 4.36 (t, *J* = 7.4 Hz, 2H, CH_2), 1.93 (p, *J* = 7.4 Hz, 2H, CH_2), 1.48 – 1.26 (m, 6H, 3 x CH_2), 0.89 (t, *J* = 7.0 Hz, 3H, CH_3).^{13}C NMR (150 MHz, $CDCl_3$) δ 151.62, 143.85, 140.96, 135.97, 131.20, 130.10, 130.03, 128.21, 126.58, 124.72, 122.75, 122.44 , 120.68, 113.61, 109.44, 97.41, 84.49, 43.63, 31.69, 29.13, 27.10, 22.71, 14.17. MS-ESI: *m/z*: calculated for $C_{40}H_{31}N_3$ $[M+H]^+$ 553.3, found 553.3.

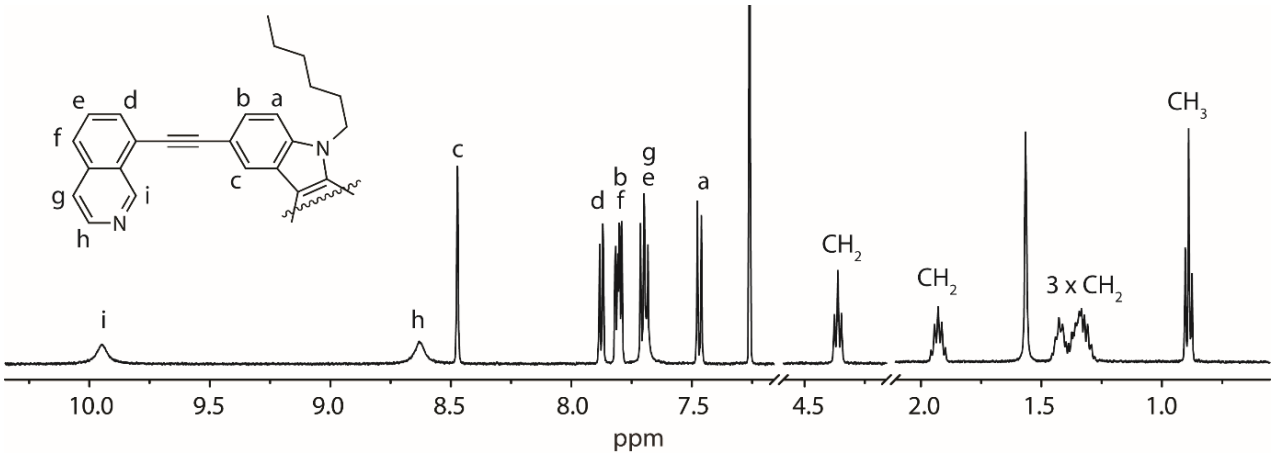

Figure S1. Partial ^{1}H NMR spectrum (500 MHz, $CDCl_3$) of **L**.

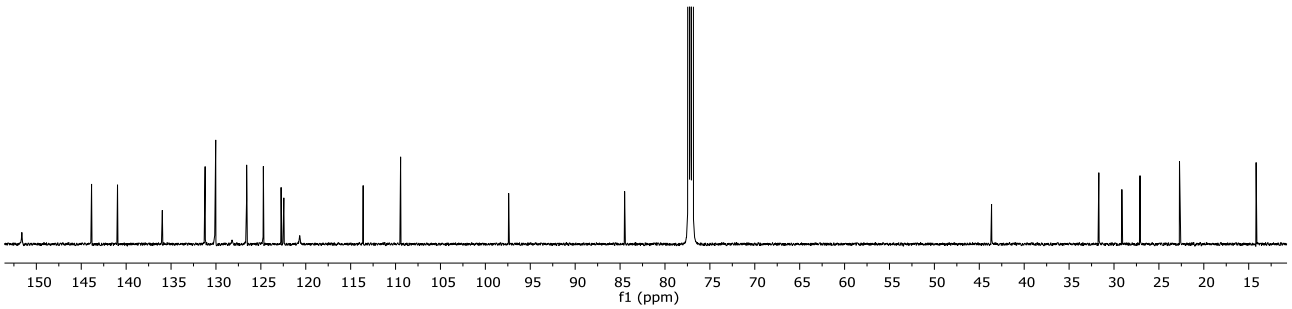

Figure S2. ^{13}C NMR spectrum (150 MHz, $CDCl_3$) of **L**.

1.3. Synthesis of Pd_2L_4 cages

General procedure: Ligand **L** (4.8 mg, 8.7 µmol) was completely dissolved in CD_3CN (2800 µL) with the aid of sonication and heating. A solution of the corresponding Pd(II) salt (300 µL, 15 mM/CD_3CN, 4.5 µmol) was subsequently added and the mixture was heated at 70 °C for various time periods to afford an orange-coloured solution of the Pd_2**L**$_4$ cage in CD_3CN.

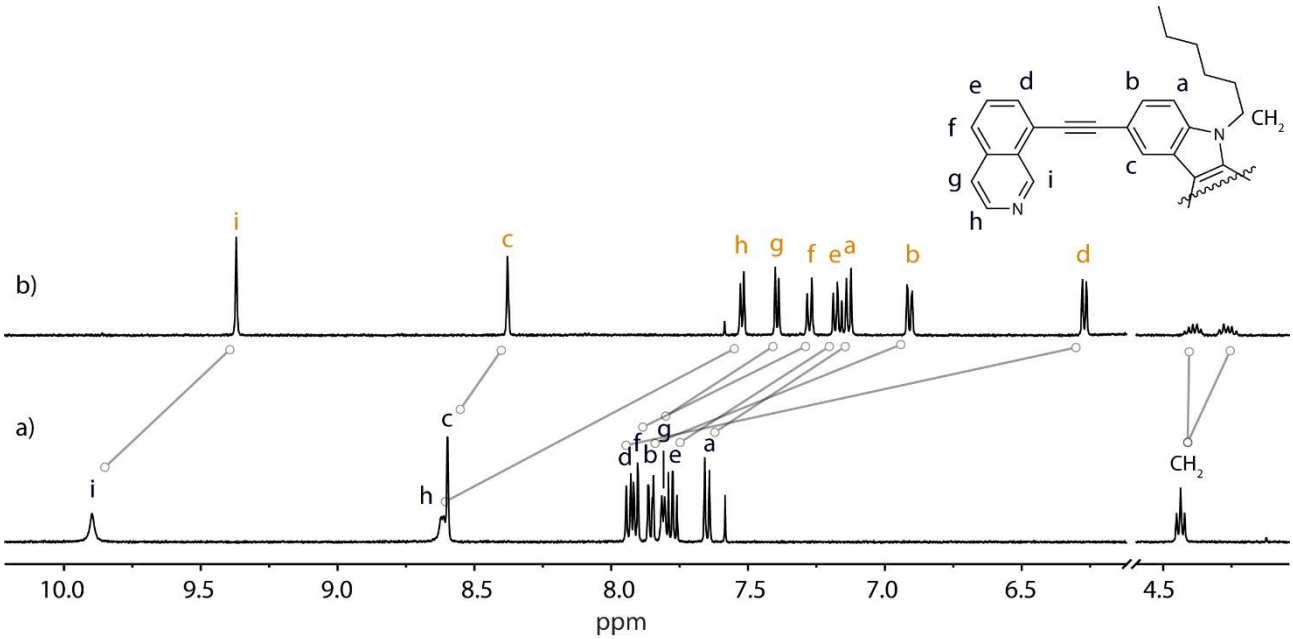

Figure S3. An example of the typical shifting observed by ^{1}H NMR spectroscopy when **L** is reacted with Pd^{II}. ^{1}H NMR spectra (500 MHz, CD_3CN): a) **L**; b) a 2:1 mixture of **L** and $[Pd(CH_3CN)_4](BF_4)_2$ heated at 70 °C for 1 h.

*1.3.1. Synthesis of $[Pd_2L_4](NO_3)_4$ (**1·NO₃**)*

$Pd(NO_3)_2$ and **L** were combined according to the general procedure and heated at 70 °C for 5 minutes to afford **1·NO₃**. ^{1}H NMR (500 MHz, CD_3CN) δ 9.26 (s, 8H, H_i), 8.60 (d, *J* = 1.6 Hz, 8H, H_c), 7.68 (d, *J* = 6.4 Hz, 8H, H_h), 7.47 (d, *J* = 6.4 Hz, 8H, H_g), 7.44 (d, *J* = 8.4 Hz, 8H, H_f), 7.31 (dd, *J* = 8.4, 7.2 Hz, 8H, H_e), 7.08 (d, *J* = 8.4 Hz, 8H, H_a), 6.73 (dd, *J* = 8.4, 1.6 Hz, 8H, H_b), 6.33 (dd, *J* = 7.2, 1.0 Hz, 8H, H_d), 4.52 – 4.37 (m, 4H, CH), 4.35 – 4.22 (m, 4H, CH), 2.10 – 1.99 (m, 8H, CH_2), 1.73 – 1.39 (m, 24H, 3 x CH_2), 1.01 (t, *J* = 7.3, 7.3 Hz, 12H, CH_3). ^{13}C NMR (151 MHz, CD_3CN) δ 156.93, 144.51, 141.06, 137.05, 134.28, 130.62, 129.15, 128.85, 126.62, 126.19, 124.64, 124.00, 123.18, 112.08, 109.51, 100.26, 81.23, 44.08, 32.32, 30.29, 27.80, 23.48, 14.39.

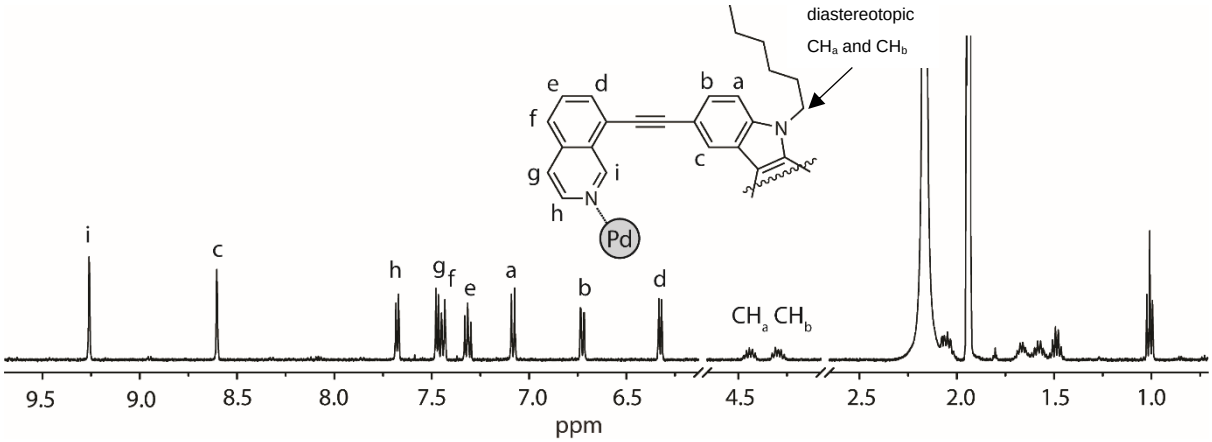

Figure S4. ^{1}H NMR spectrum (500 MHz, CD_3CN) of **1·NO₃**

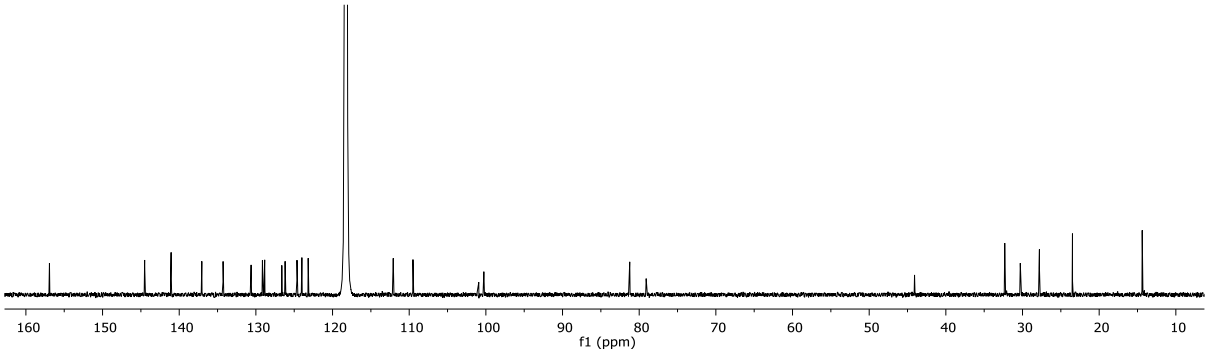

Figure S5. ^{13}C NMR spectrum (150 MHz, CD_3CN) of **1·NO₃**.

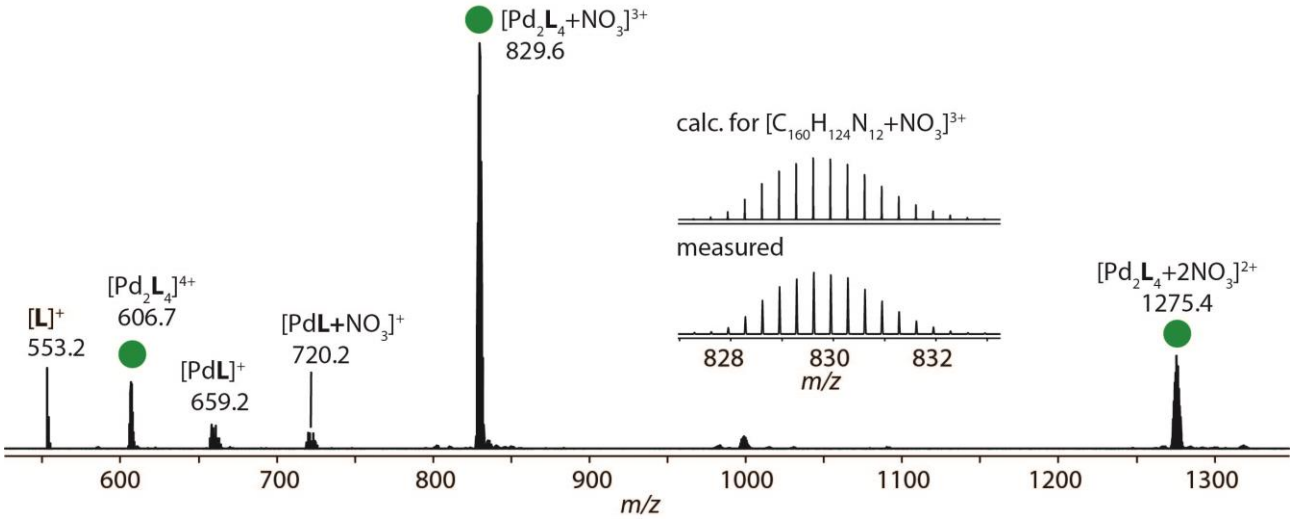

Figure S6. ESI-MS spectrum of **1·NO$_3$**. The spectrum shows peaks of $[Pd_2\mathbf{L}_4+n NO_3]^{4-n+}$ (n = 0−2) and the measured and calculated isotope pattern of $[Pd_2\mathbf{L}_4+NO_3]^{3+}$ is also shown.

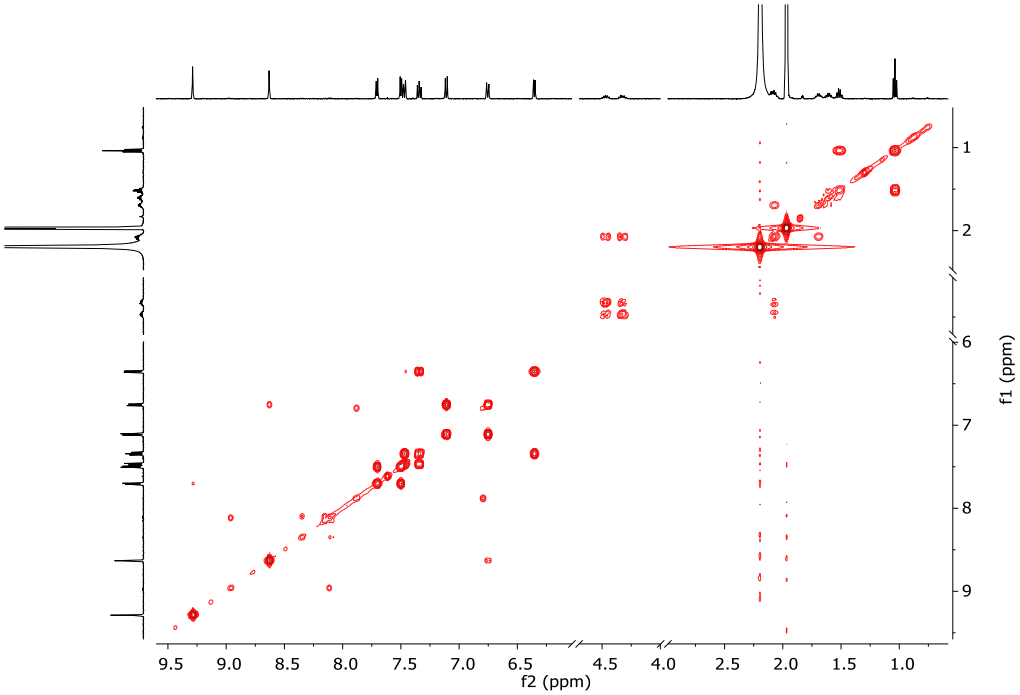

Figure S7. ^{1}H – ^{1}H COSY spectrum (600 MHz/CD_3CN) of **1·NO$_3$**.

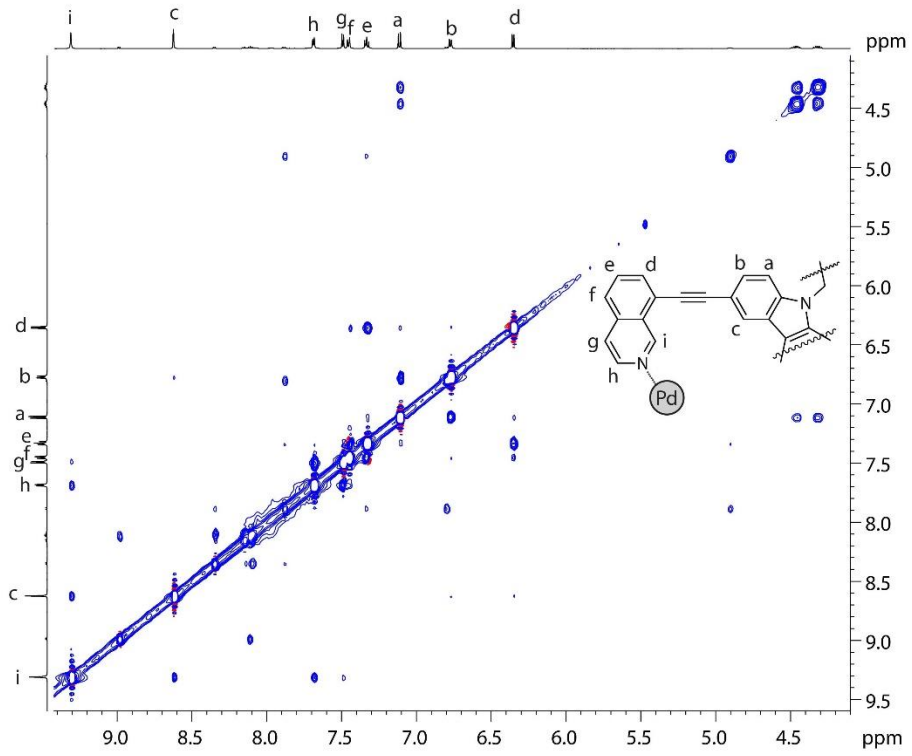

Figure S8. ^{1}H – ^{1}H NOESY spectrum (600 MHz/CD_3CN) of **1·NO_3**.

*1.3.2. Synthesis of [BF_4@Pd_2**L**$_4$](BF_4)$_3$ (**1·BF_4**)*

[Pd(CH_3CN)$_4$](BF_4)$_2$ and **L** were combined according to the general procedure and heated at 70 °C for 1 h to afford **1·BF_4**. ^{1}H NMR (500 MHz, CD_3CN) δ 9.37 (s, 8H, H_i), 8.38 (d, *J* = 1.6 Hz, 8H, H_c), 7.52 (d, *J* = 6.4 Hz, 8H, H_h), 7.39 (d, *J* = 6.4 Hz, 8H, H_g), 7.28 (d, *J* = 8.4 Hz, 8H, H_f), 7.17 (dd, *J* = 8.4, 7.2 Hz, 8H, H_e), 7.13 (d, *J* = 8.4 Hz, 8H, H_a), 6.91 (dd, *J* = 8.3, 1.6 Hz, 8H, H_b), 6.27 (dd, *J* = 7.2, 1.0 Hz, 8H, H_d), 4.47 – 4.32 (m, 4H, CH), 4.32 – 4.20 (m, 4H, CH), 2.08 – 1.99 (m, 8H, CH_2), 1.72 – 1.63 (m, 8H, CH_2), 1.63 – 1.55 (m, 8H, CH_2), 1.55 – 1.44 (m, 8H, CH_2), 1.03 (t, *J* = 7.3, 7.3 Hz, 12H, CH_3). ^{13}C NMR (101 MHz, CD_3CN) δ 157.43, 144.59, 140.99, 137.17, 134.10, 130.14, 129.41, 128.67, 127.04, 125.76, 124.70, 123.64, 123.36, 112.35, 109.38, 101.05, 81.80, 44.07, 32.34, 30.29, 27.85, 23.52, 14.43. ^{19}F NMR (377 MHz, CD_3CN) δ −149.35 (4F, br, encapsulated BF_4^-), −151.79 (12F, free BF_4^-).

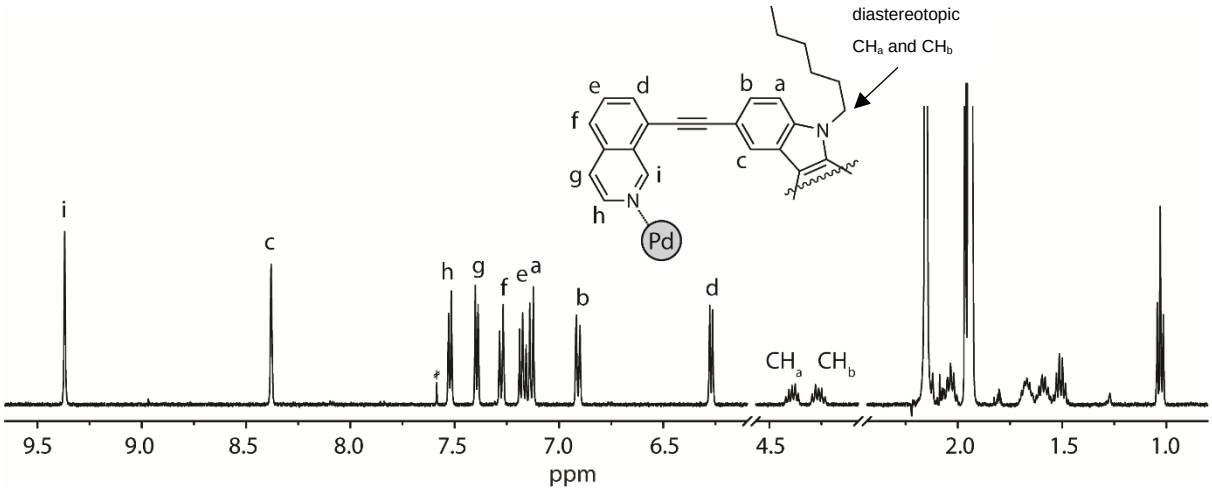

Figure S9. Partial ^{1}H NMR spectrum (500 MHz, CD_3CN) of **1·BF_4**.

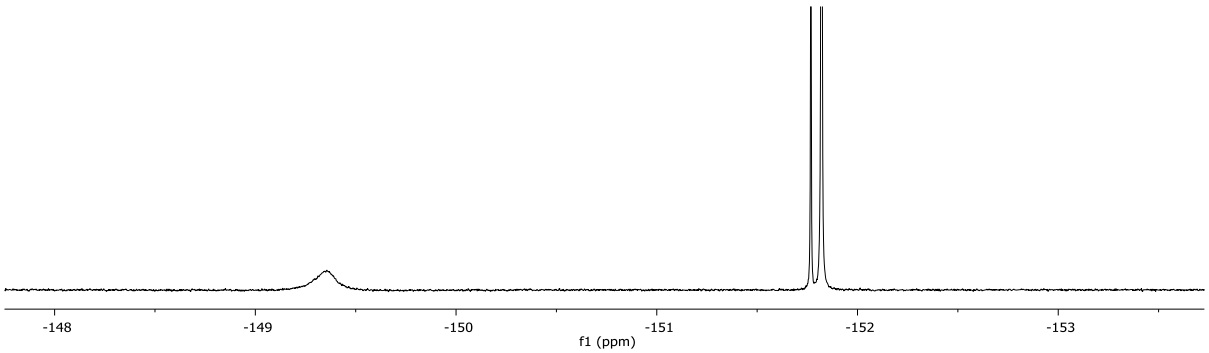

Figure S10. ^{19}F NMR spectrum (377 MHz, CD_3CN) of **1·BF$_4$**. δ −149.35 (4F, br, encapsulated BF_4^-), −151.79 (12F, free BF_4^-).

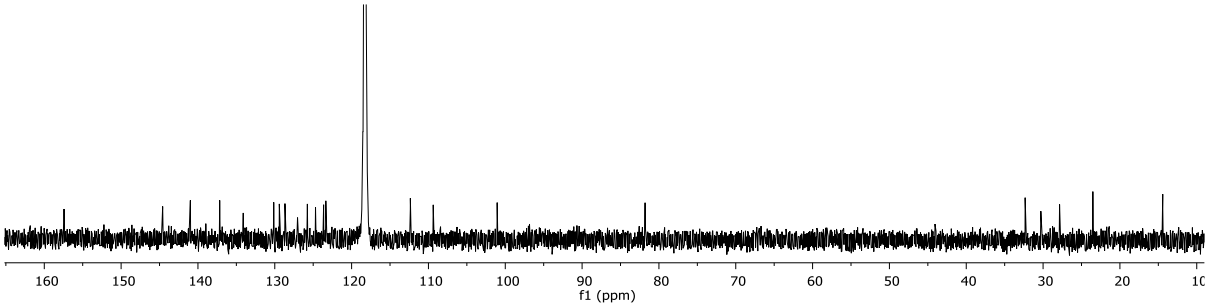

Figure S11. ^{13}C NMR spectrum (150 MHz, CD_3CN) of **1·BF$_4$**.

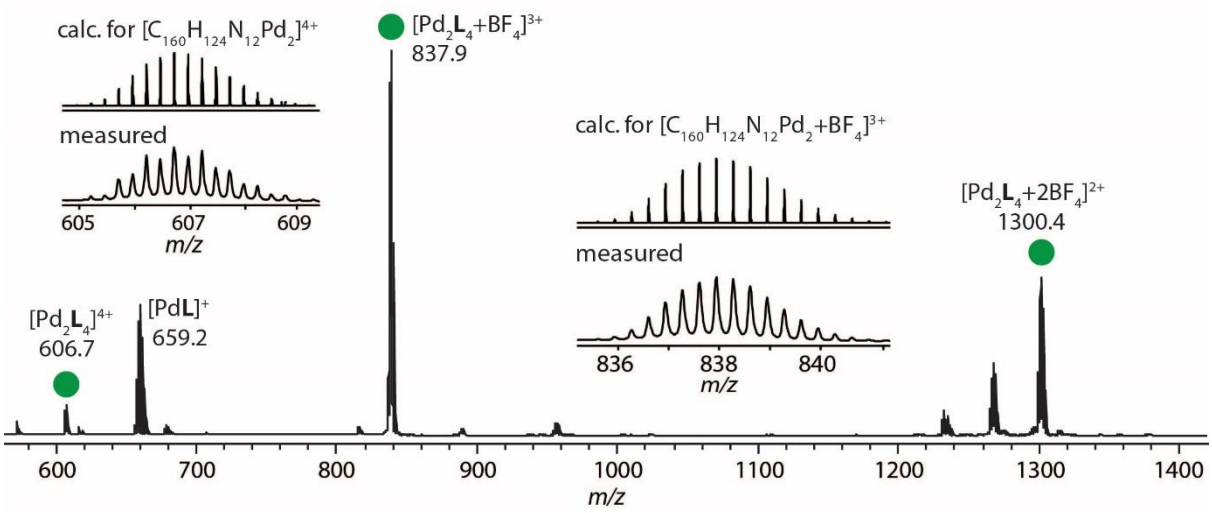

Figure S12. ESI-MS spectrum of **1·BF$_4$**. The spectrum shows peaks of $[Pd_2\mathbf{L}_4+n\mathrm{BF}_4]^{4-n+}$ (n = 0−2) and the measured and calculated isotope patterns of $[Pd_2\mathbf{L}_4]^{4+}$ and $[Pd_2\mathbf{L}_4+\mathrm{BF}_4]^{3+}$ are shown.

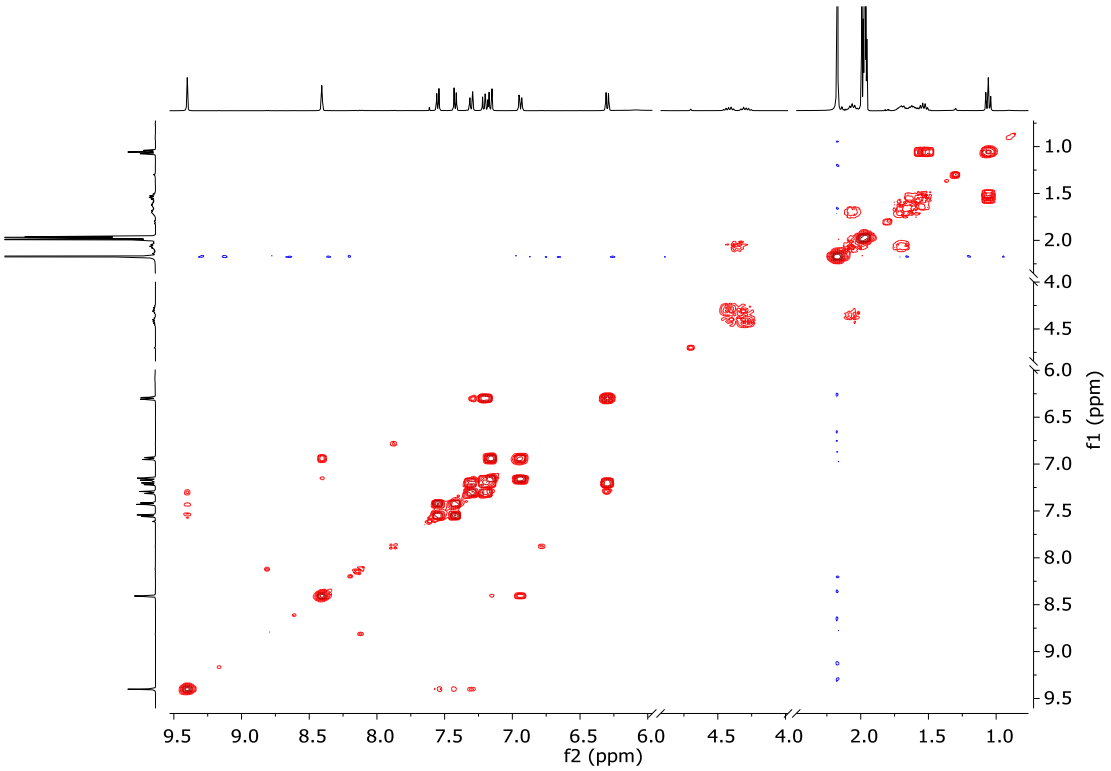

Figure S13. ^{1}H – ^{1}H COSY spectrum (600 MHz/CD_3CN) of **1·BF_4**.

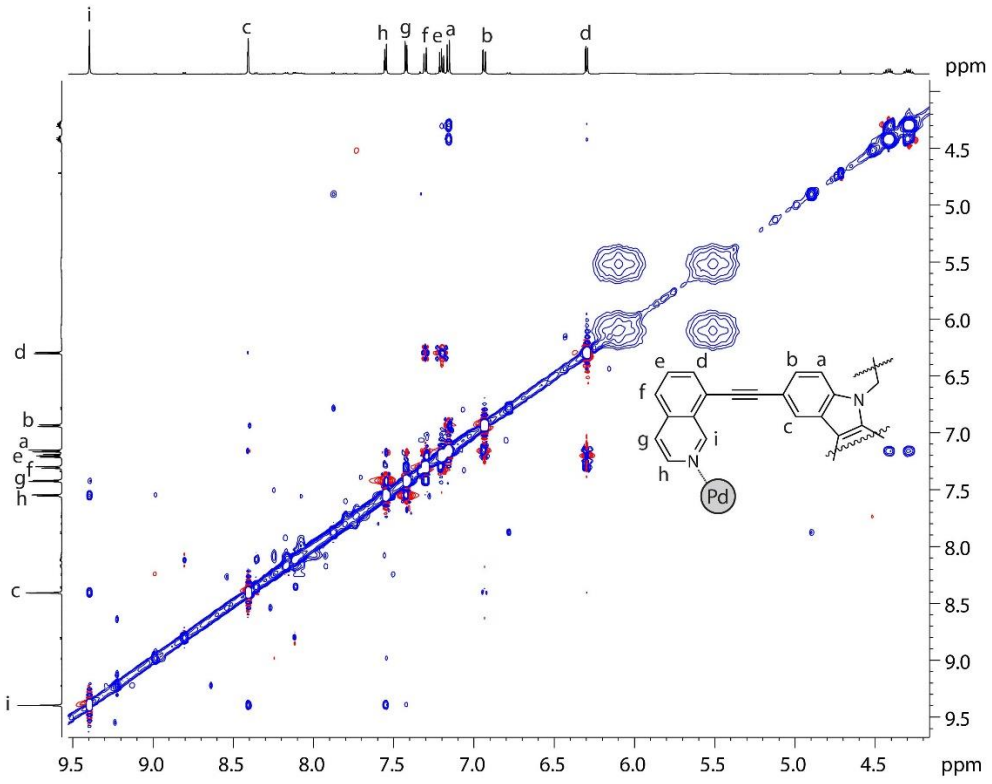

Figure S14. ^{1}H – ^{1}H NOESY spectrum (600 MHz/CD_3CN) of **1·BF_4**.

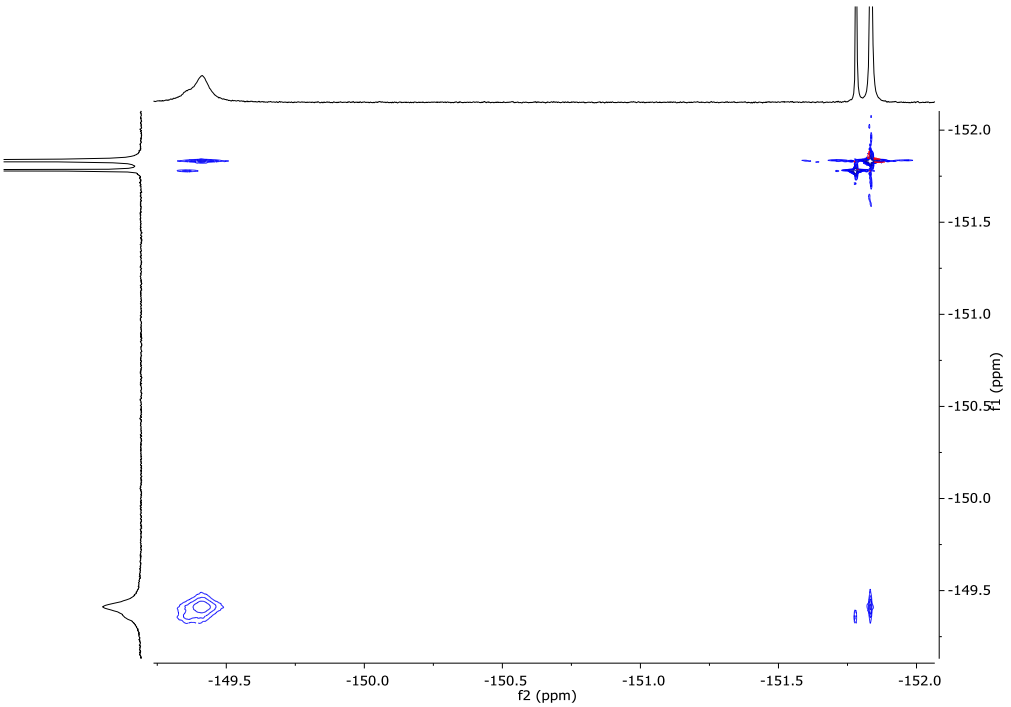

Figure S15. $^{19}F - {}^{19}F$ EXSY spectrum (600 MHz/CD_3CN, 25 °C) of **1·BF_4**. δ −149.35 (4F, br, encapsulated BF_4^-), −151.79 (12F, free BF_4^-). Exchange between the free and encapsulated BF_4^- is observed.

*1.3.3. Synthesis of [ClO_4@Pd_2**L**$_4$](ClO_4)$_3$ (**1·ClO_4**)*

$[Pd(CH_3CN)_4](ClO_4)_2$ and **L** were combined according to the general procedure and heated at 70 °C for 1 h to afford **1·ClO_4**. ^1H NMR (700 MHz, CD_3CN) δ 9.42 (s, 8H, H_i), 8.31 (d, *J* = 1.4 Hz, 8H, H_c), 7.52 (d, *J* = 6.2 Hz, 8H, H_h), 7.38 (d, *J* = 6.2 Hz, 8H, H_g), 7.23 (d, *J* = 8.3 Hz, 8H, H_f), 7.16 (d, *J* = 8.3 Hz, 8H, H_a), 7.12 (dd, *J* = 8.3, 7.3 Hz, 8H, H_e), 6.97 (dd, *J* = 8.3, 1.4 Hz, 8H, H_b), 6.25 (d, *J* = 7.3 Hz, 8H, H_d), 4.43 – 4.21 (m, 8H, CH_2), 2.07 – 2.00 (m, 8H, CH_2), 1.71 – 1.55 (m, 16H, 2 x CH_2), 1.55 – 1.46 (m, 8H, CH_2), 1.03 (t, *J* = 7.3 Hz, 12H, CH_3). ^{13}C NMR (175 MHz, CD_3CN) δ 157.65, 144.71, 141.01, 137.22, 134.03, 130.14, 129.45, 128.64, 127.14, 125.69, 124.66, 123.49, 123.38, 112.45, 109.44, 101.08, 82.04, 44.08, 32.34, 30.29, 27.87, 23.53, 14.43.

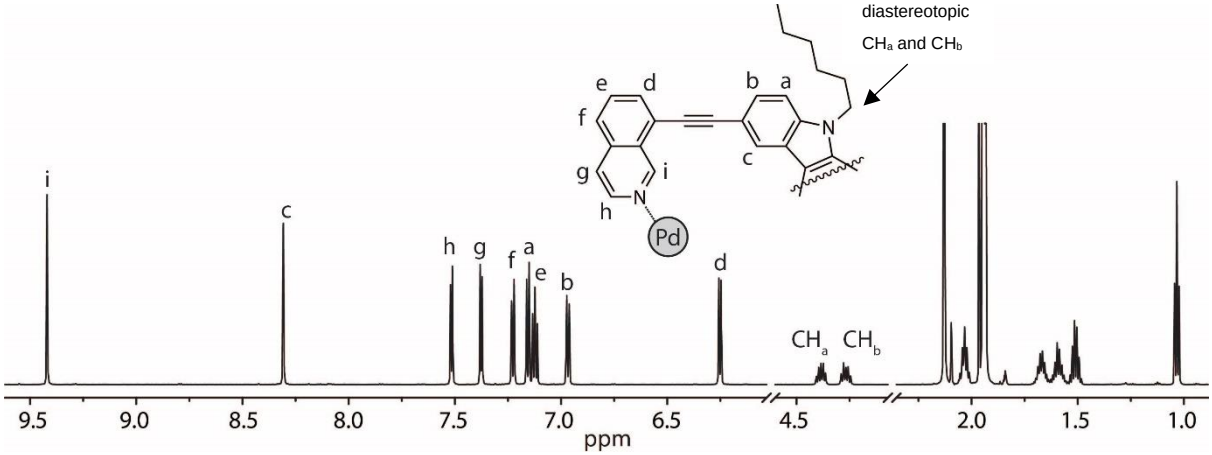

Figure S16. Partial ^1H NMR spectrum (700 MHz, CD_3CN) of **1·ClO_4**.

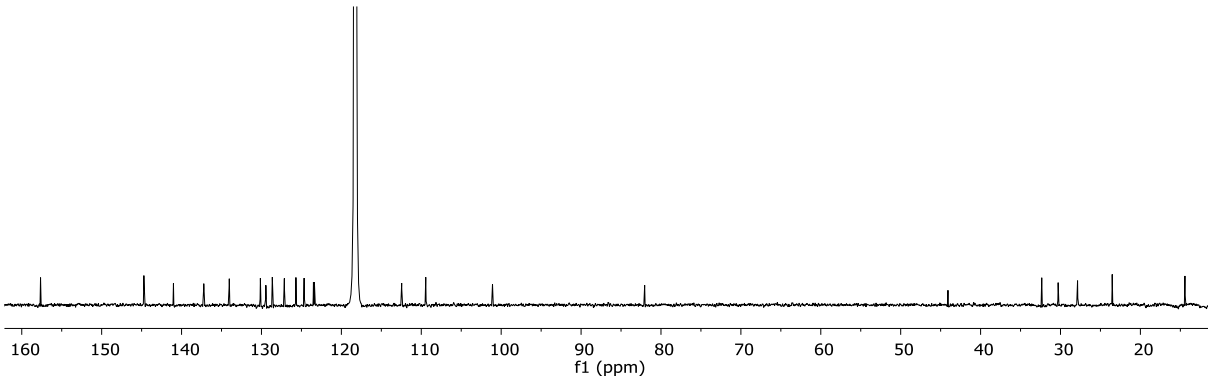

Figure S17. ^{13}C NMR spectrum (150 MHz, CD_3CN) of **1·ClO$_4$**.

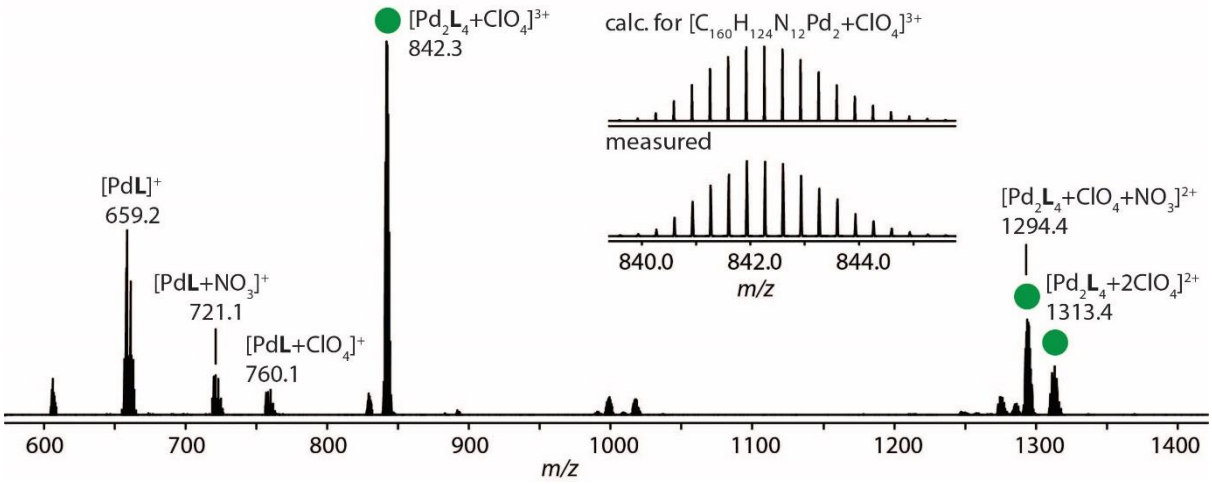

Figure S18. ESI-MS spectrum of **1·ClO$_4$**. The spectrum shows peaks of $[Pd_2\mathbf{L}_4+n\mathrm{ClO}_4]^{4-n+}$ (n = 1, 2) and the measured and calculated isotope pattern of $[Pd_2\mathbf{L}_4+\mathrm{ClO}_4]^{3+}$ is also shown.

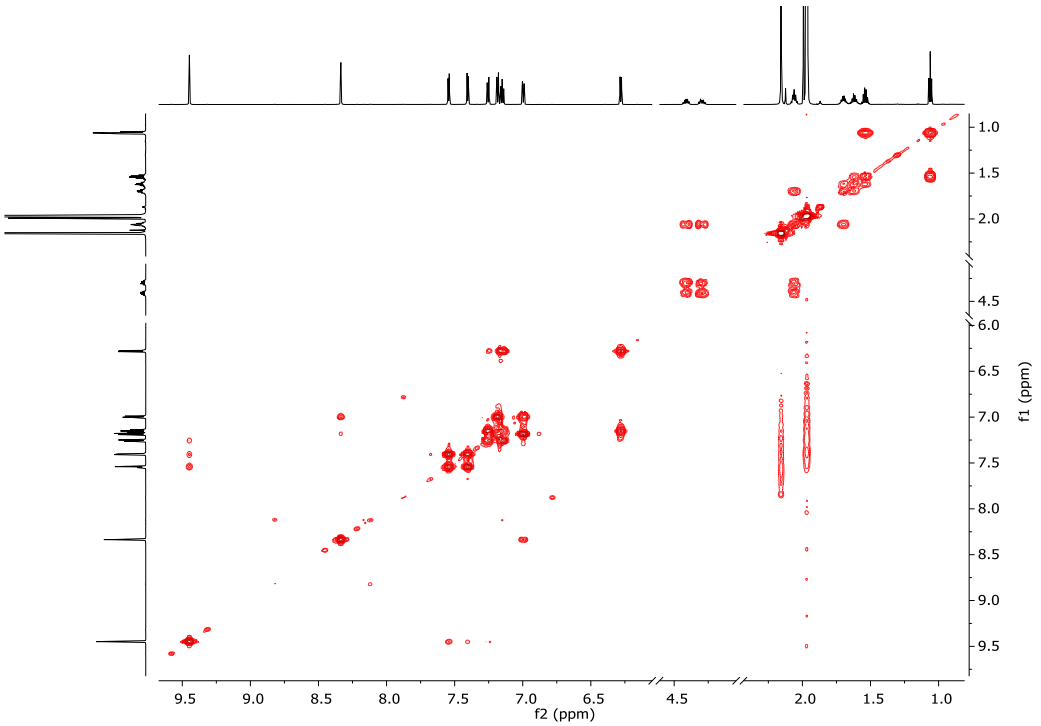

Figure S19. ^{1}H – ^{1}H COSY spectrum (600 MHz/CD_3CN) of **1·ClO$_4$**.

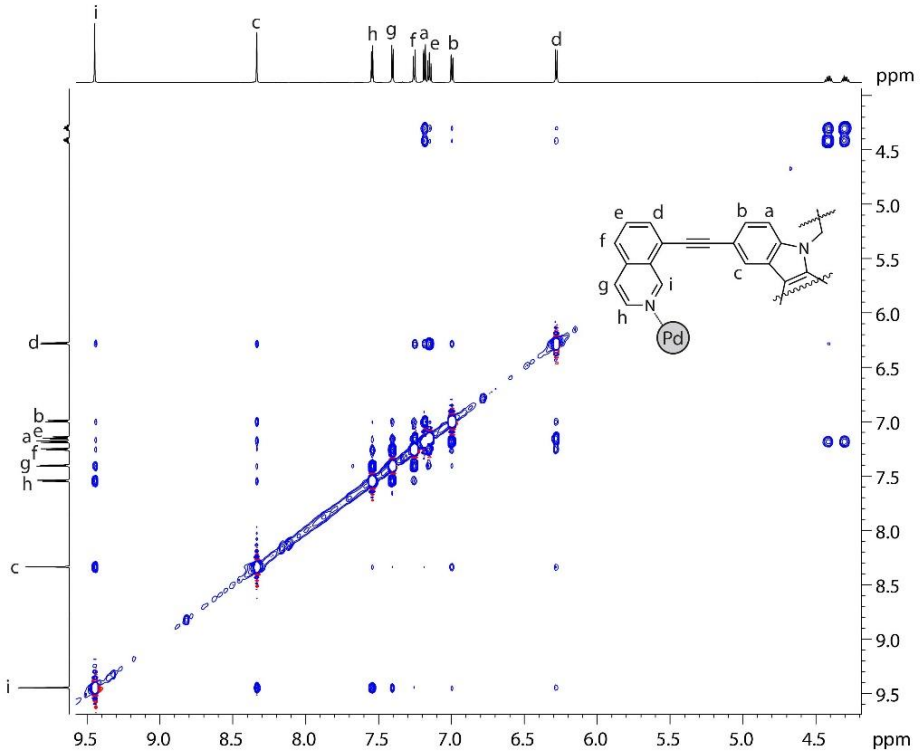

Figure S20. ^{1}H – ^{1}H NOESY spectrum (600 MHz/CD_3CN) of **1·ClO$_4$**.

*1.3.4. Synthesis of [PF$_6$@Pd$_2$**L**$_4$](PF$_6$)$_3$ (**1·PF$_6$**)*

[Pd(CH_3CN)$_4$](PF$_6$)$_2$ and **L** were combined according to the general procedure and heated at 70 °C for 1 h to afford **1·PF$_6$**. ^{1}H NMR (500 MHz, CD_3CN) δ 9.35 (s, 8H, H$_i$), 8.15 (d, *J* = 1.6 Hz, 8H, H$_c$), 7.56 (d, *J* = 6.4 Hz, 8H, H$_h$), 7.38 (d, *J* = 6.4 Hz, 8H, H$_g$), 7.19 (dd, *J* = 8.4, 6.2 Hz, 16H, H$_f$, H$_a$), 7.07 (dd, *J* = 8.4, 7.2 Hz, 8H, H$_e$), 7.01 (dd, *J* = 8.3, 1.6 Hz, 8H, H$_b$), 6.22 (dd, *J* = 7.2, 1.0 Hz, 8H, H$_d$), 4.47 – 4.35 (m, 4H, CH), 4.34 – 4.24 (m, 4H, CH), 2.07 – 2.01 (m, 8H, CH_2), 1.73 – 1.63 (m, 8H, CH_2), 1.63 – 1.54 (m, 8H, CH_2), 1.55 – 1.44 (m, 8H, CH_2), 1.03 (t, *J* = 7.2, 7.2 Hz, 12H, CH_3). ^{13}C NMR (150 MHz, CD_3CN) δ 157.63, 144.84, 140.98, 137.21, 133.91, 130.32, 129.34, 128.52, 126.75, 125.65, 124.58, 123.35, 123.30, 112.41, 109.41, 100.74, 79.09, 44.04, 32.33, 30.27, 27.85, 23.51, 14.42. ^{19}F NMR (377 MHz, CD_3CN) δ -66.46 (d, *J* = 718.8 Hz, 6F, encapsulated PF_6^-), -72.96 (d, *J* = 706.6 Hz, 18F, free PF_6^-).

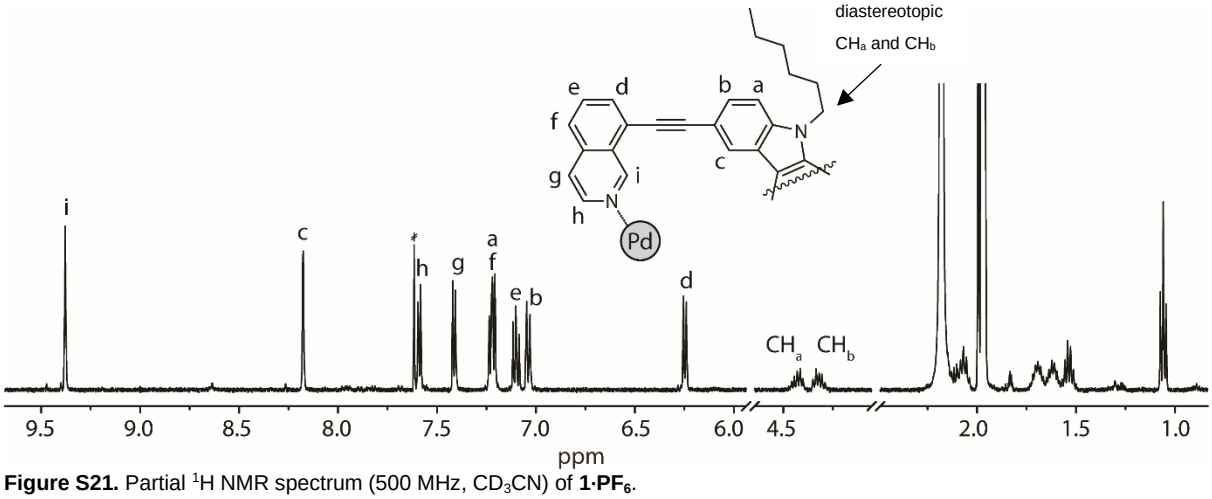

Figure S21. Partial ^{1}H NMR spectrum (500 MHz, CD_3CN) of **1·PF$_6$**.

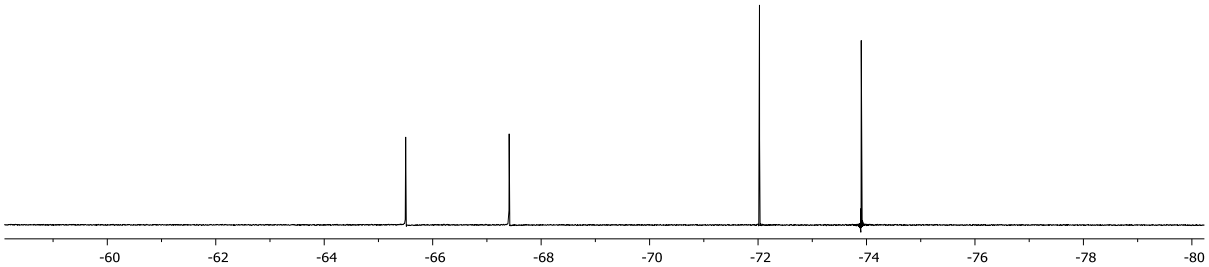

Figure S22. ^{19}F NMR spectrum (377 MHz, CD_3CN) of **1·PF$_6$**. δ -66.46 (d, J = 718.8 Hz, 6F, encapsulated PF_6^-), -72.96 (d, J = 706.6 Hz, 18F, free PF_6^-).

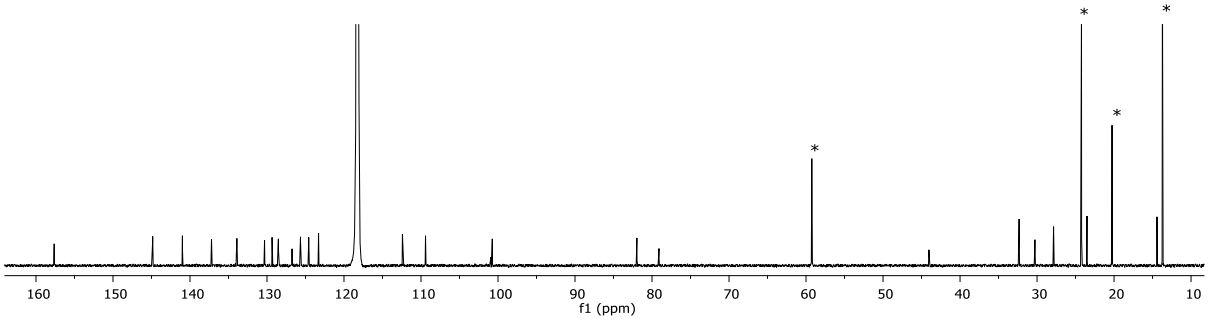

Figure S23. ^{13}C NMR spectrum (150 MHz, CD_3CN) of **1·PF$_6$** obtained by treating $[Pd_2\mathbf{L}_4]^{4+}$ with 1.1 equiv. of *t*BuNPF$_6$ (due to problems obtaining a sample of sufficient concentration directly from the $[Pd(CH_3CN)](PF_6)_2$ salt). Signals marked with the * correspond to tetrabutylammonium carbon atoms.

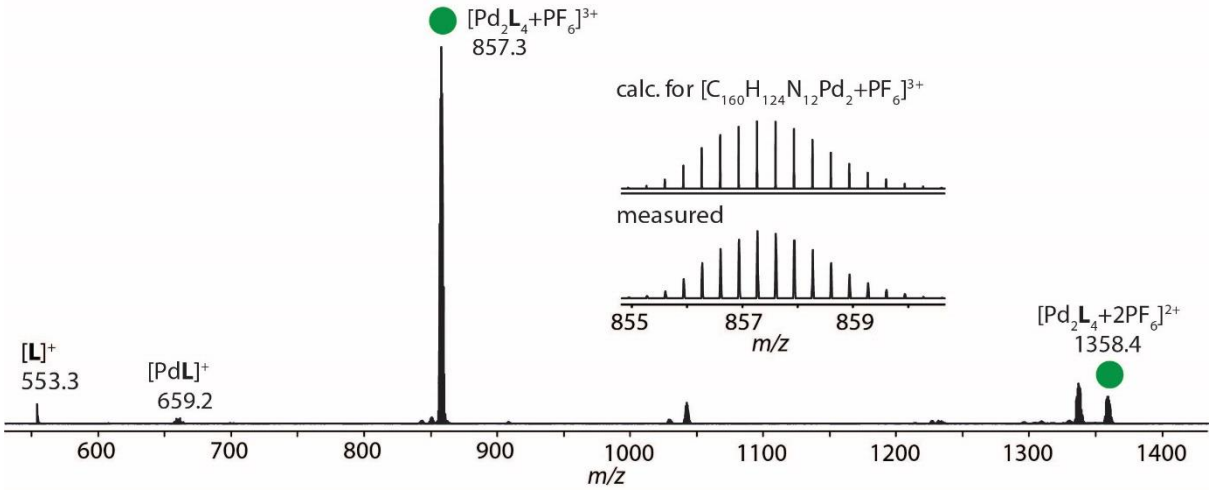

Figure S24. ESI-MS spectrum of **1·PF$_6$**. The spectrum shows peaks of $[Pd_2\mathbf{L}_4{+}n\mathrm{PF}_6]^{4-n+}$ (n = 1, 2) and the measured and calculated isotope pattern of $[Pd_2\mathbf{L}_4{+}\mathrm{PF}_6]^{3+}$ is also shown.

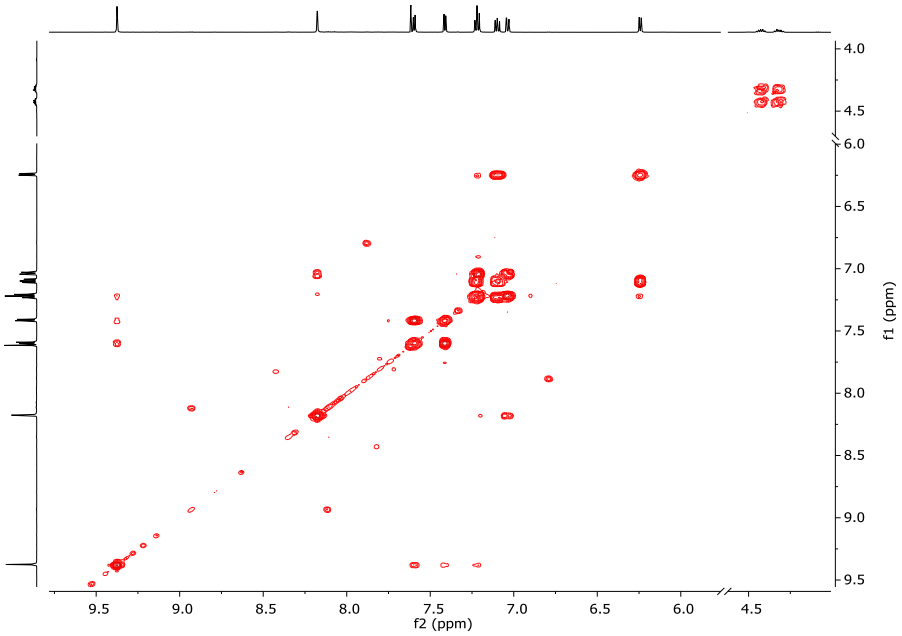

Figure S25. ^{1}H – ^{1}H COSY spectrum (600 MHz, CD_3CN) of **1·PF_6**.

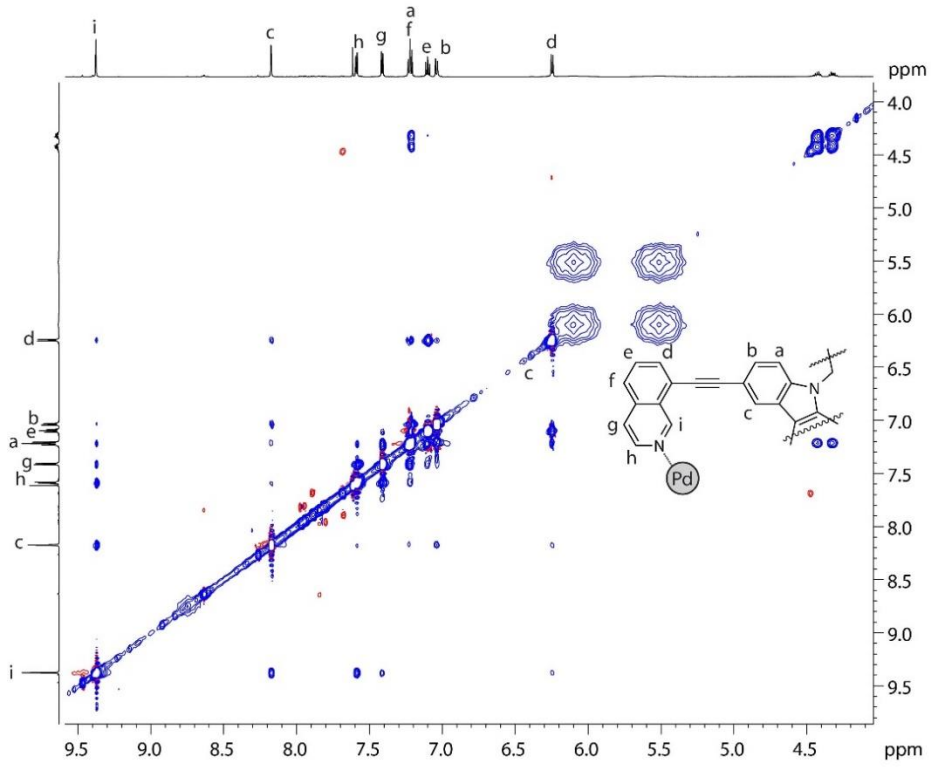

Figure S26. ^{1}H – ^{1}H NOESY spectrum (600 MHz, CD_3CN) of **1·PF_6**.

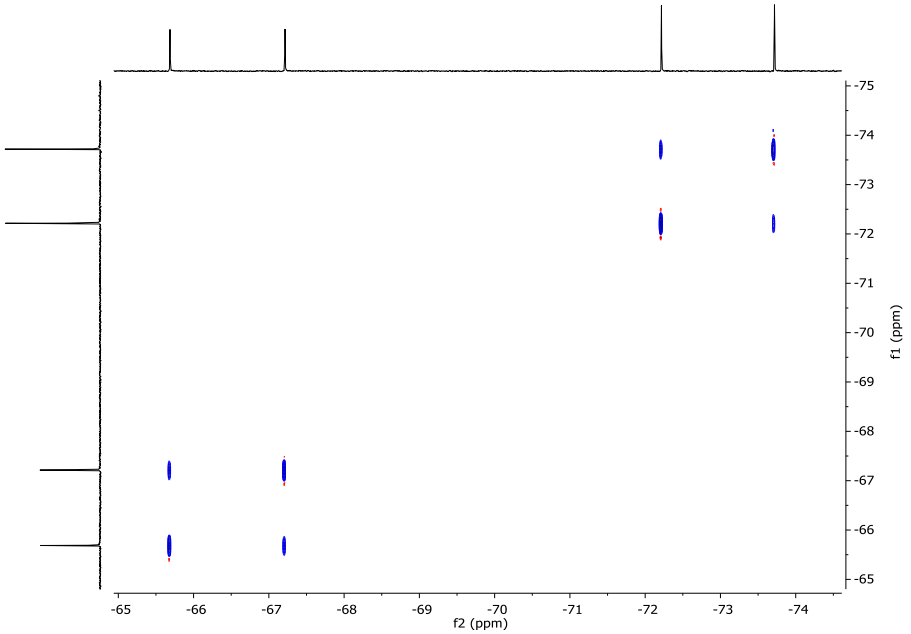

Figure S27. ^{19}F – ^{19}F EXSY spectrum (565 MHz, CD_3CN, 25 °C) of **1·PF$_6$**. δ −66.46 (d, J = 718.8 Hz, 6F, encapsulated PF_6^-), -72.96 (d, J = 706.6 Hz, 18F, free PF_6^-). No exchange between the encapsulated and free is PF_6^- is observed under the conditions of the measurement.

*1.3.5. Synthesis of [OTf@Pd$_2$**L**$_4$](OTf)$_3$ (**1·OTf**)*

$[Pd(CH_3CN)_4](OTf)_2$ and **L** were combined according to the general procedure and heated at 70 °C for 1 h to afford **1·OTf**. ^1H NMR (500 MHz, CD_3CN) δ 9.30 (s, 8H), 8.29 (d, 8H), 7.67 (d, *J* = 6.4 Hz, 8H), 7.44 (d, *J* = 6.4 Hz, 8H), 7.28 (d, *J* = 8.4 Hz, 8H), 7.18 (d, *J* = 8.4 Hz, 8H), 7.13 (dd, *J* = 8.4, 7.3 Hz, 8H), 6.94 (dd, *J* = 8.4, 1.6 Hz, 8H), 6.22 (d, *J* = 7.3, 8H, H_d), 4.54 – 4.19 (m, 8H), 2.09 – 2.01 (m, 8H), 1.71 – 1.54 (m, 16H), 1.55 – 1.45 (m, 8H), 1.02 (t, *J* = 7.2 Hz, 12H). ^{13}C NMR (150 MHz, CD_3CN) δ 157.86, 144.81, 141.01, 137.19, 134.11, 130.71, 129.18, 128.64, 126.80, 125.90, 124.61, 123.49, 123.37, 112.20, 109.43, 100.23, 81.53, 44.05, 32.33, 30.28, 27.84, 23.50, 14.41. ^{19}F NMR (565 MHz, CD_3CN) δ −71.96 (s, 3F, encapsulated OTf^-) , −79.34 (s, 9H, free OTf^-) .

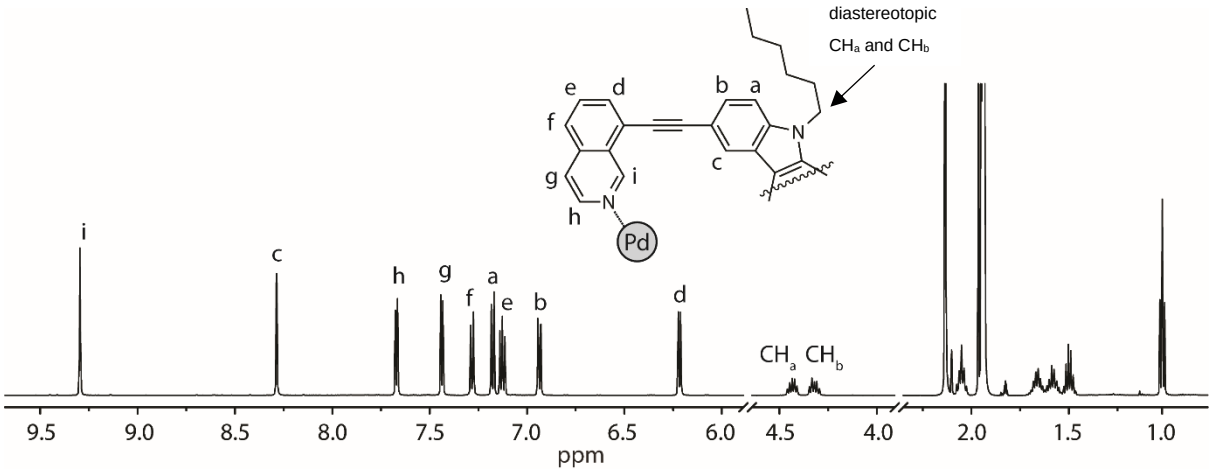

Figure S28. Partial ^1H NMR spectrum (500 MHz, CD_3CN) of **1·OTf**.

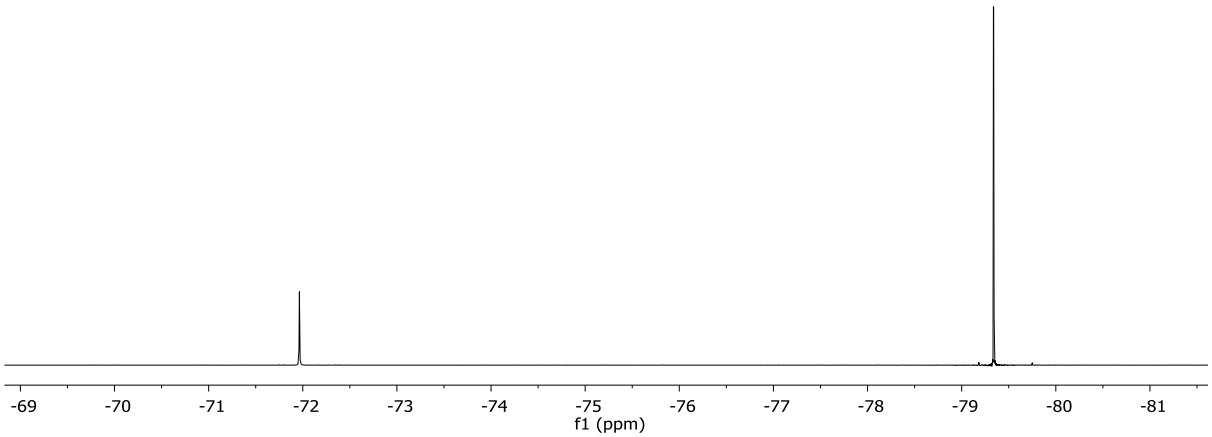

Figure S29. ^{19}F NMR spectrum (377 MHz, CD_3CN) of **1·OTf**. δ −71.96 (s, 3F, encapsulated OTf^-) , −79.34 (s, 9H, free OTf^-) . δ −71.96 (s, 3F, encapsulated OTf^-) , −79.34 (s, 9H, free OTf^-)

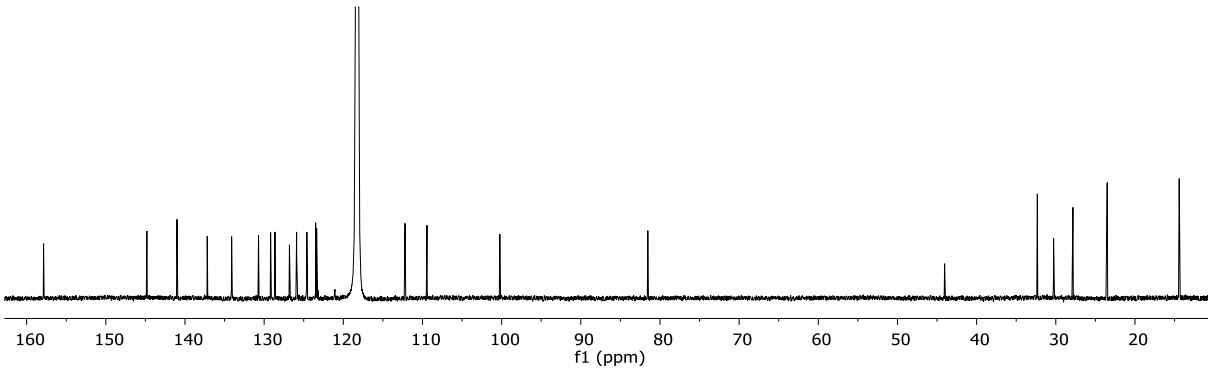

Figure S30. ^{13}C NMR spectrum (150 MHz, CD_3CN) of **1·OTf**.

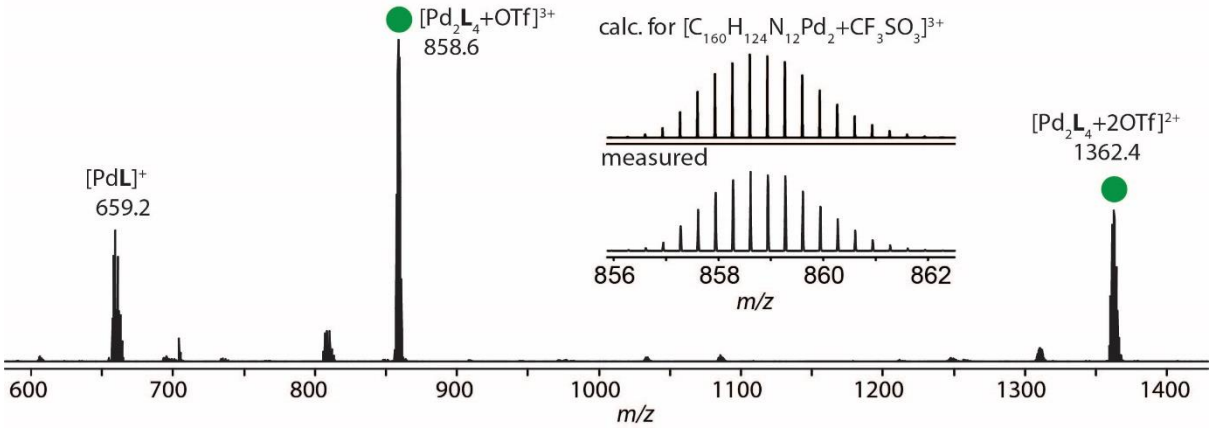

Figure S31. ESI-MS spectrum of **1·OTf**. The spectrum shows peaks of $[Pd_2\mathbf{L}_4+n\text{OTf}]^{4-n+}$ (n = 1, 2) and the measured and calculated isotope pattern of $[Pd_2\mathbf{L}_4+\text{OTf}]^{3+}$ is also shown.

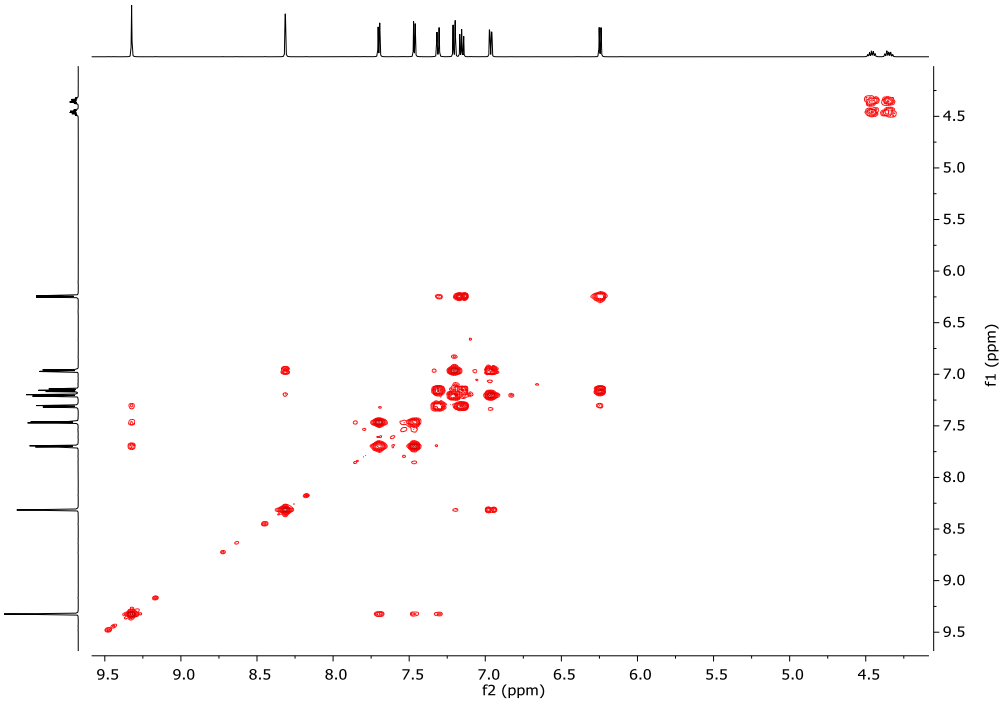

Figure S32. ^{1}H – ^{1}H COSY spectrum (600 MHz, CD_3CN) of **1·OTf**.

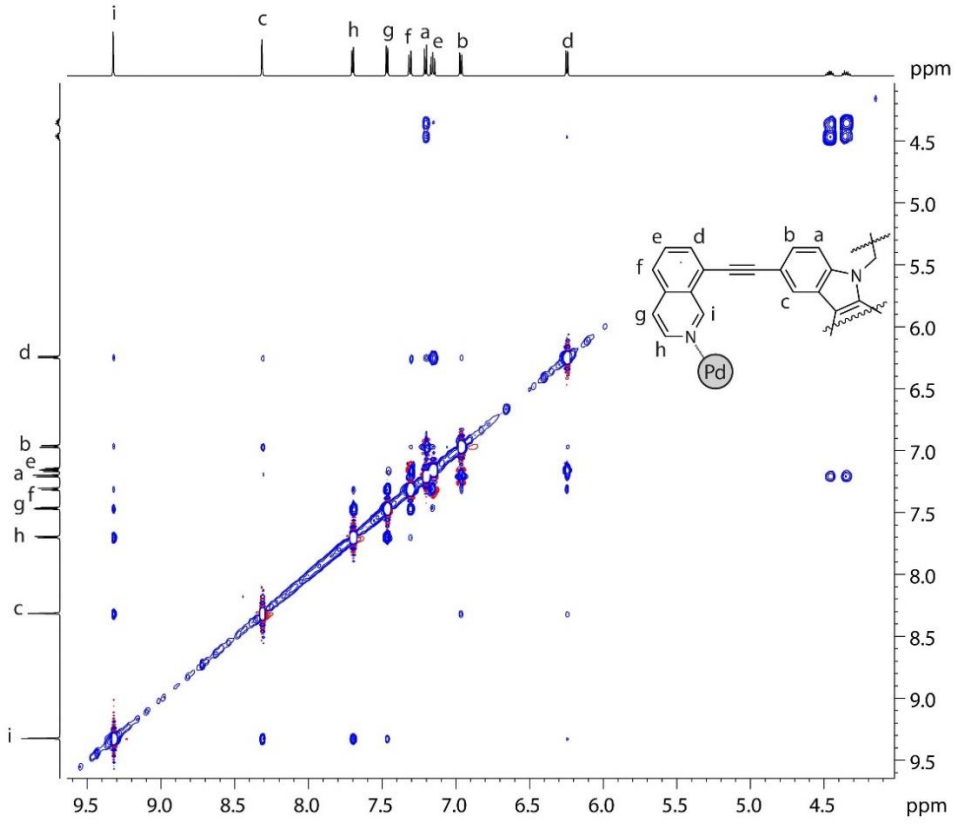

Figure S33. ^{1}H – ^{1}H NOESY spectrum (600 MHz, CD_3CN) of **1·OTf**.

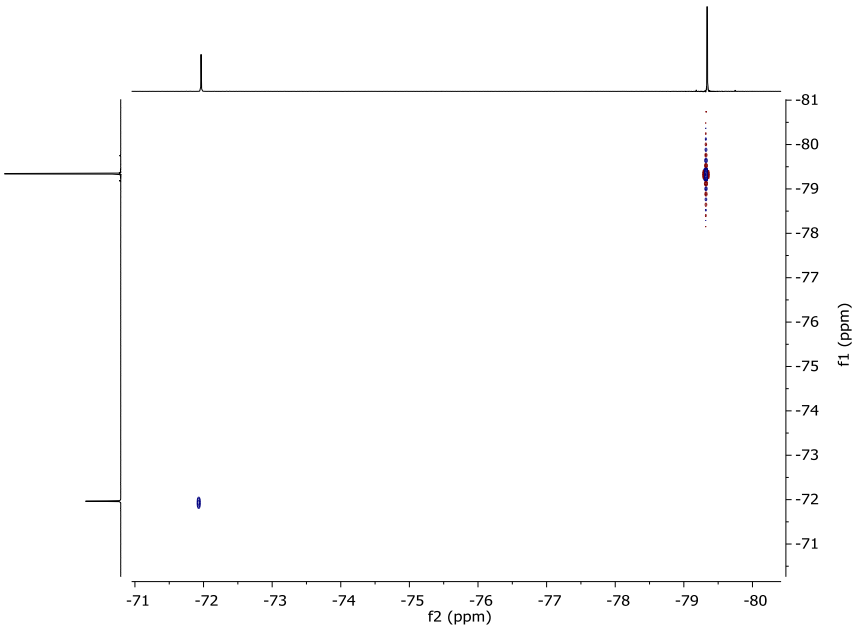

Figure S34. ^{19}F – ^{19}F ESXY spectrum (565 MHz, CD_3CN, 25 °C) of **1·OTf**. δ −71.96 (s, 3F, encapsulated OTf^-) , −79.34 (s, 9H, free OTf^-) . δ −71.96 (s, 3F, encapsulated OTf^-), −79.34 (s, 9H, free OTf^-). No exchange between the encapsulate and free OTf^- is observed under the conditions of the measurement.

*1.3.6. Synthesis of $[SbF_6@Pd_2L_4](SbF_6)_3$ (**1·SbF₆**)*

$[Pd(CH_3CN)_4](SbF_6)_2$ and **L** were combined according to the general procedure and heated at 70 °C for 1 h to afford **1·SbF₆**. ^1H NMR (600 MHz, CD_3CN) δ 9.30 (s, 8H, H_i), 8.04 (d, J = 1.6 Hz, 8H, H_c), 7.64 (d, J = 6.4 Hz, 8H, H_h), 7.40 (d, J = 6.4 Hz, 8H, H_g), 7.23 (d, J = 8.4 Hz, 8H, H_a), 7.17 (d, J = 8.3 Hz, 8H, H_f), 7.06 (dd, J = 8.4, 1.6 Hz, 8H, H_b), 7.01 (dd, J = 8.3, 7.3 Hz, 8H, H_e), 6.19 (d, J = 7.3, 8H, H_d), 4.51 – 4.22 (m, 8H, CH_2), 2.09 – 2.00 (m, 8H, CH_2), 1.71 – 1.54 (m, 16H, 2 x CH_2), 1.50 (h, J = 7.0 Hz, 8H, CH_2), 1.02 (t, J = 7.3 Hz, 12H, CH_3). ^{13}C NMR (150 MHz, CD_3CN) δ 157.87, 144.98, 141.04, 137.26, 133.87, 130.74, 129.24, 128.48, 126.44, 125.69, 124.58, 123.39, 123.15, 112.43, 109.48, 100.32, 81.93, 44.05, 32.33, 30.27, 27.85, 23.51, 14.41.

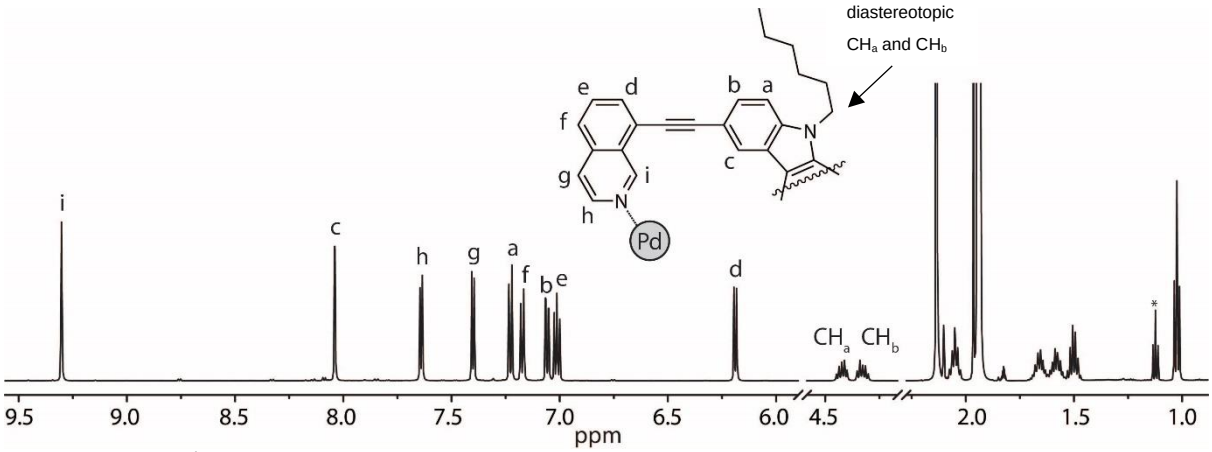

Figure S35. Partial ^1H NMR spectrum (600 MHz, CD_3CN) of **1·SbF₆** (* = diethyl ether).

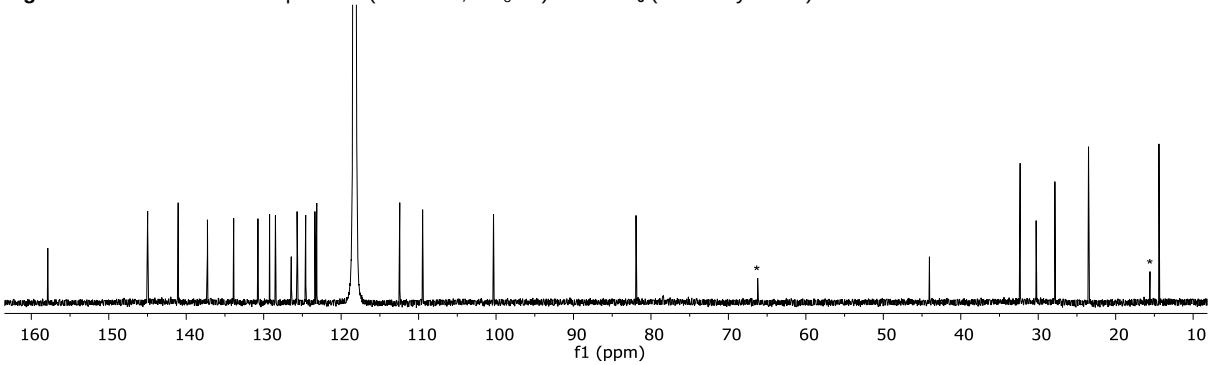

Figure S36. ^{13}C NMR spectrum (150 MHz, CD_3CN) of **1·SbF₆**. (* = diethyl ether).

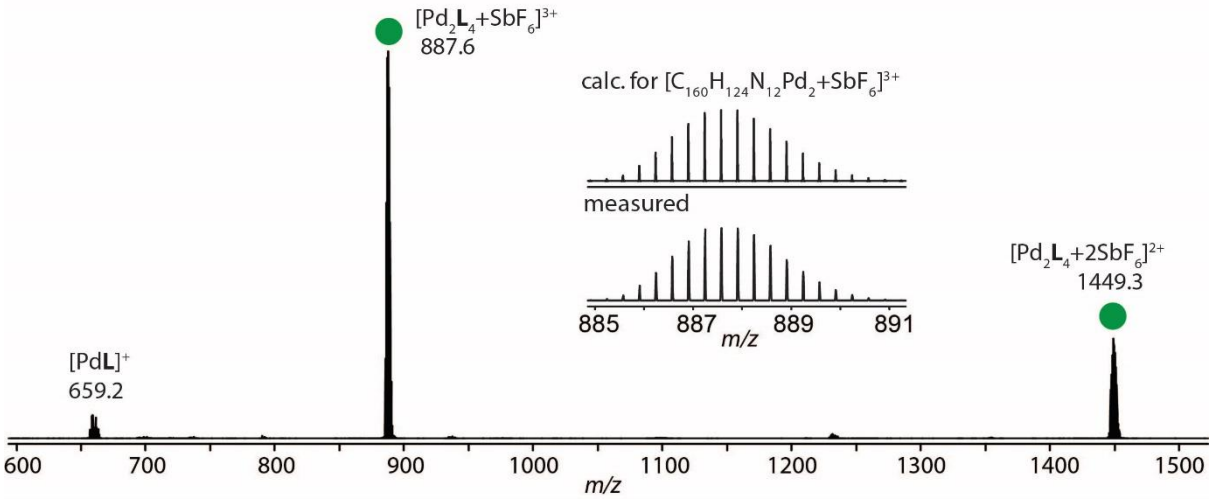

Figure S37. ESI-MS spectrum of **1·SbF$_6$**. The spectrum shows peaks of $[Pd_2\mathbf{L}_4+n\mathrm{SbF}_6]^{4-n+}$ (n = 1, 2) and the measured and calculated isotope pattern of $[Pd_2\mathbf{L}_4+\mathrm{SbF}_6]^{3+}$ is also shown.

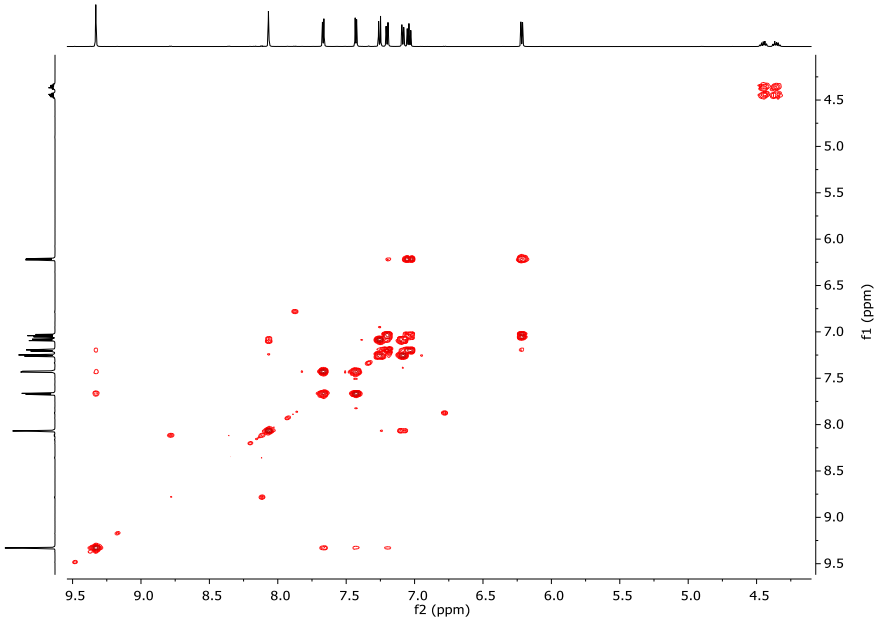

Figure S38. ^{1}H – ^{1}H COSY spectrum (600 MHz, CD_3CN) of **1·SbF$_6$**.

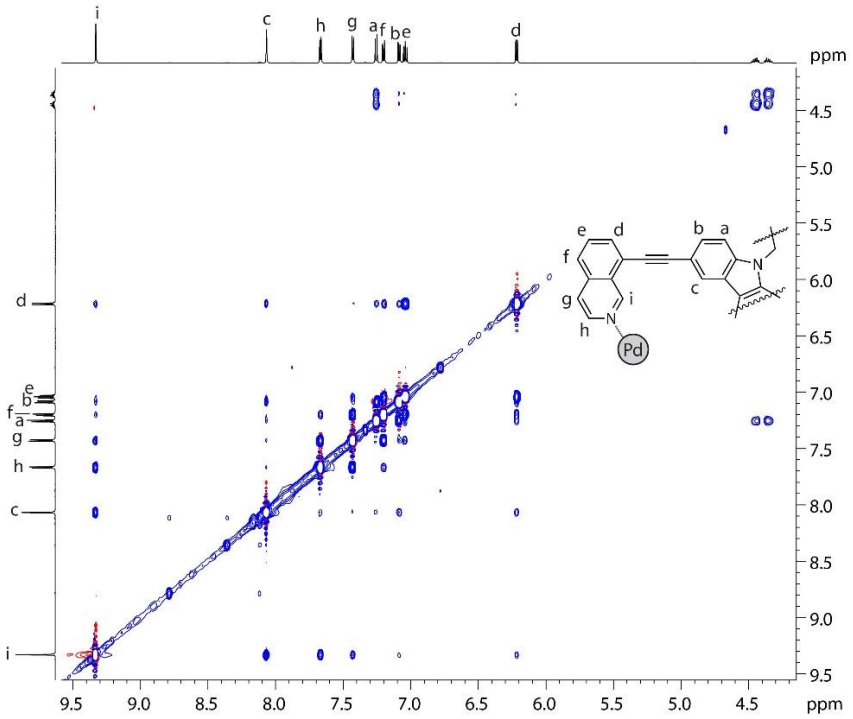

Figure S39. ^{1}H – ^{1}H NOESY spectrum (600 MHz, C_3CN) of **1·SbF$_6$**.

*1.3.7. Synthesis of [ReO$_4$@Pd$_2$**L**$_4$](NO$_3$)$_3$ (**1·ReO$_4$**)*

To a sample of [Pd$_2$**L**$_4$](NO$_3$)$_4$ (0.7 mM, 600 µL, CD_3CN), 1.1 equivalents of tetrabutylammonium perrhenate was added at 25 °C to immediately give **1·ReO$_4$**. ^{1}H NMR (500 MHz, CD_3CN) δ 9.46 (s, 8H, H$_i$), 8.20 (d, *J* = 1.6 Hz, 8H, H$_c$), 7.58 (d, *J* = 6.4 Hz, 8H, H$_h$), 7.38 (d, *J* = 6.4 Hz, 8H, H$_g$), 7.25 – 7.12 (m, 16H, H$_f$, H$_a$), 7.10 – 6.99 (m, 16H, H$_e$, H$_b$), 6.22 (d, *J* = 7.3 Hz, 8H, H$_d$), 4.49 – 4.12 (m, 8H, CH_2), 2.07 – 2.00 (m, 8H, CH_2), 1.72 – 1.56 (m, 16H, 2 x CH_2), 1.54 – 1.45 (m, 8H, CH_2), 1.03 (t, *J* = 7.2 Hz, 12H, CH_3).

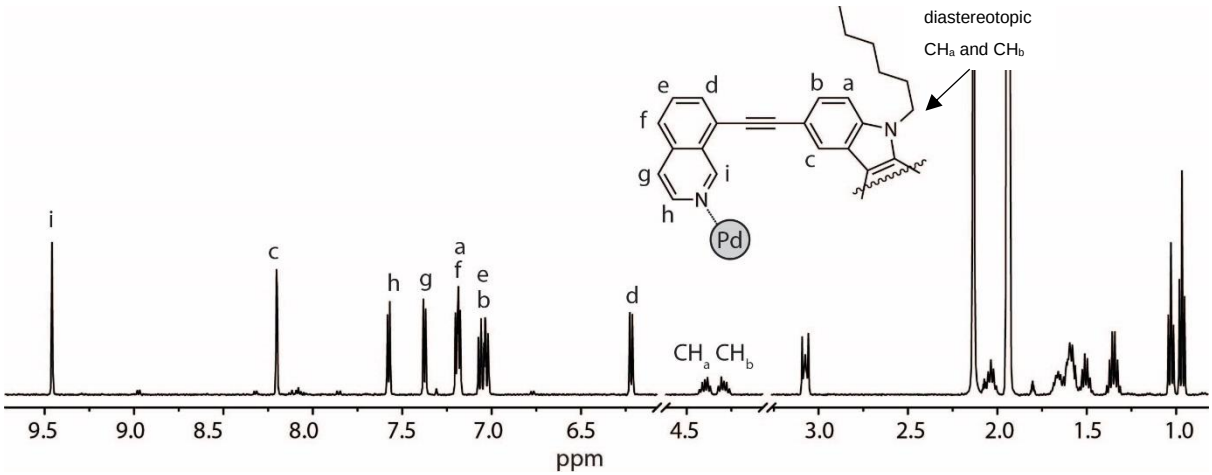

Figure S40. Partial ^{1}H NMR spectrum (500 MHz, CD_3CN) of **1·ReO$_4$** obtained by the addition of 1.1 equivalents of tetrabutylammonium perrhenate to a sample of [Pd$_2$**L**$_4$](NO$_3$)$_4$ in CD_3CN.

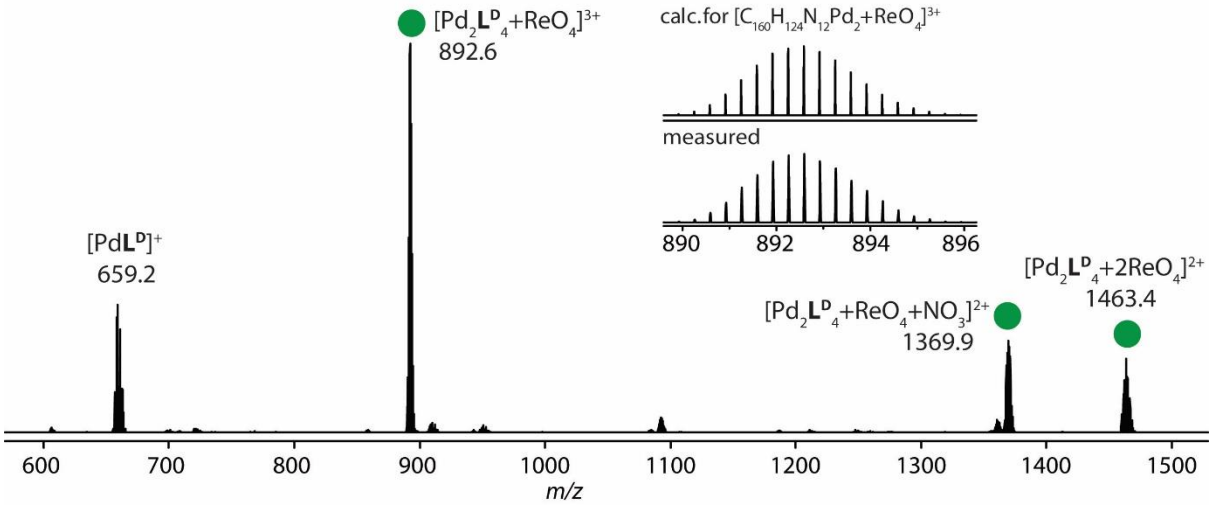

Figure S41. ESI-MS spectrum of **1·ReO₄.** The spectrum shows peaks of $[Pd_2\mathbf{L}_4+n\mathrm{ReO}_4]^{4-n+}$ (n = 1, 2) and the measured and calculated isotope pattern of $[Pd_2\mathbf{L}_4+\mathrm{ReO}_4]^{3+}$ is also shown.

*1.3.8. Synthesis of $[Pd_2\mathbf{L}_4]\cdot(NTf_2)_4$ (**1/1'**)*

$[Pd(CH_3CN)_4](NTf_2)_2$ and **L** were combined according to the general procedure without heating to afford a 4:1 mixture of the chiral and achiral forms (**1** and **1'**) of $[Pd_2\mathbf{L}_4]^{4+}$ as a yellow solution. ^{1}H NMR (500 MHz, CD_3CN) **1**: δ 9.41 (s, 8H, H_i), 8.70 (d, J = 1.5 Hz, 8H, H_c), 7.76 (d, J = 6.4 Hz, 8H, H_h), 7.55 – 7.49 (m, 16H, H_f, H_g), 7.40 (dd, J = 8.4, 7.3 Hz, 8H, H_e), 7.07 (d, J = 8.5 Hz, 8H, H_a), 6.63 (dd, J = 8.5, 1.5 Hz, 8H, H_b), 6.38 (d, J = 7.3 Hz, 8H, H_d), 4.59 – 4.24 (m, 8H, N-CH_2), 2.09 – 2.02 (m, 8H, CH_2), 1.72 – 1.42 (m, 24H, 3xCH_2), 0.99 (t, J = 7.3 Hz, 12H, CH_3); **1'**: δ 9.86 (s, 8H, $H_{i'}$), 8.75 (d, J = 6.6 Hz, 8H, $H_{h'}$), 8.33 (d, J = 7.0 Hz, 8H, $H_{d'}$), 8.14 (d, J = 8.2 Hz, 8H, $H_{f'}$), 8.12 – 8.05 (m, 16H, $H_{e'}$, $H_{g'}$), 7.85 (d, J = 8.5 Hz, 8H, $H_{a'}$), 7.31 (d, J = 1.5 Hz, 8H, $H_{c'}$), 6.75 (d, J = 8.5 Hz, 8H, $H_{b'}$), 4.88 (t, J = 7.4 Hz, 8H, N-CH_2), 1.82 – 1.77 (m, 8H, CH_2), 0.73 (t, J = 7.3 Hz, 12H, CH_3), other CH_2 signals overlap with alkyl signals of **1**.

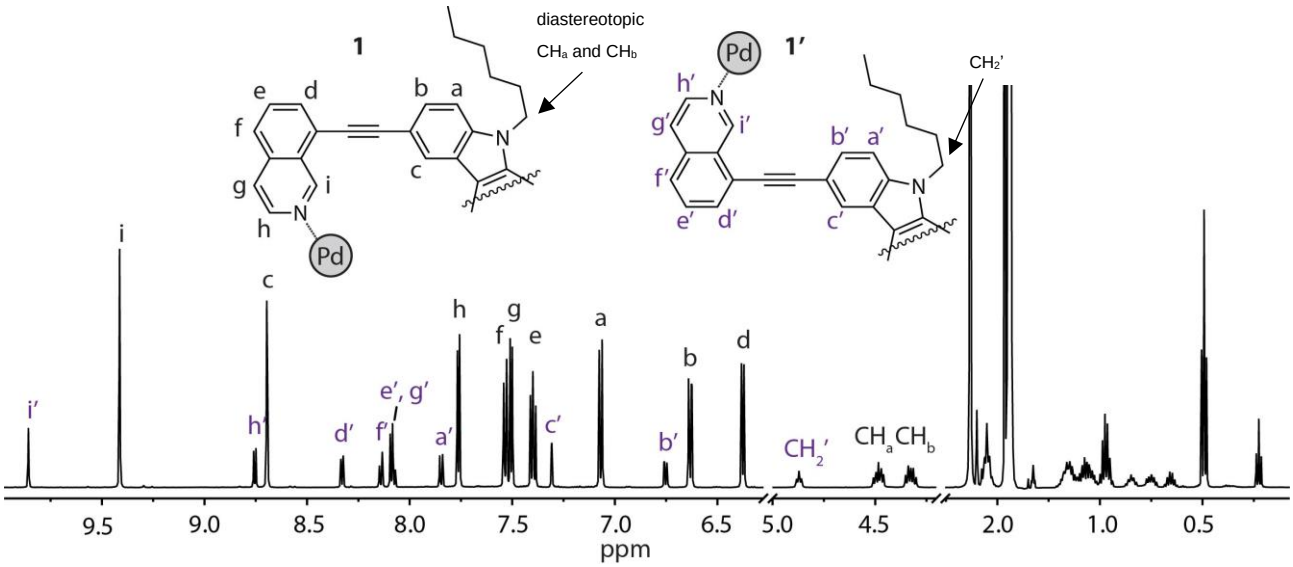

Figure S42. Partial ^{1}H NMR spectrum (500 MHz, CD_3CN) of a 4:1 mixture of the helicate $[Pd_2\mathbf{L}_4]\cdot(NTf_2)_4$ (**1**) and mesocate $[Pd_2\mathbf{L}_4]\cdot(NTf_2)_4$ (**1'**).

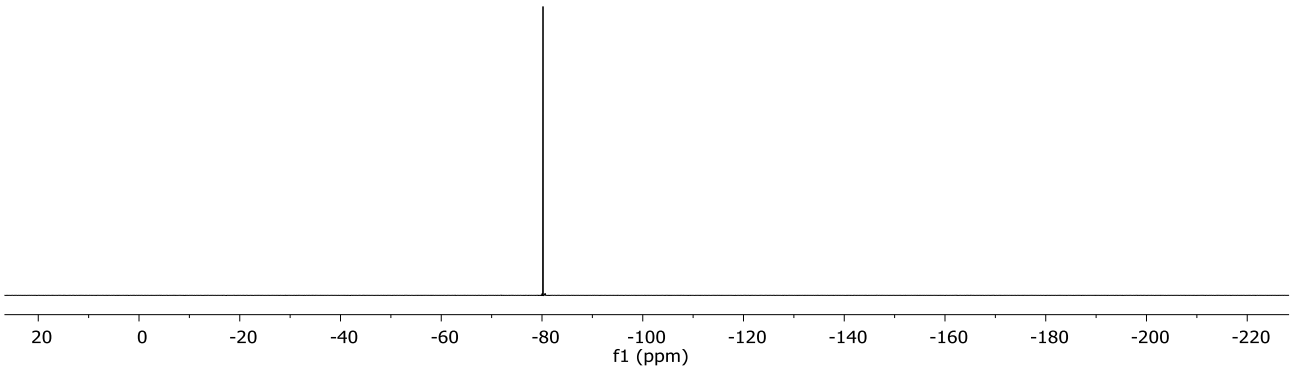

Figure S43. ^{19}F NMR spectrum (565 MHz, CD_3CN) of the mixture of **1/1'**. δ −80.22 (free NTf_2^-).

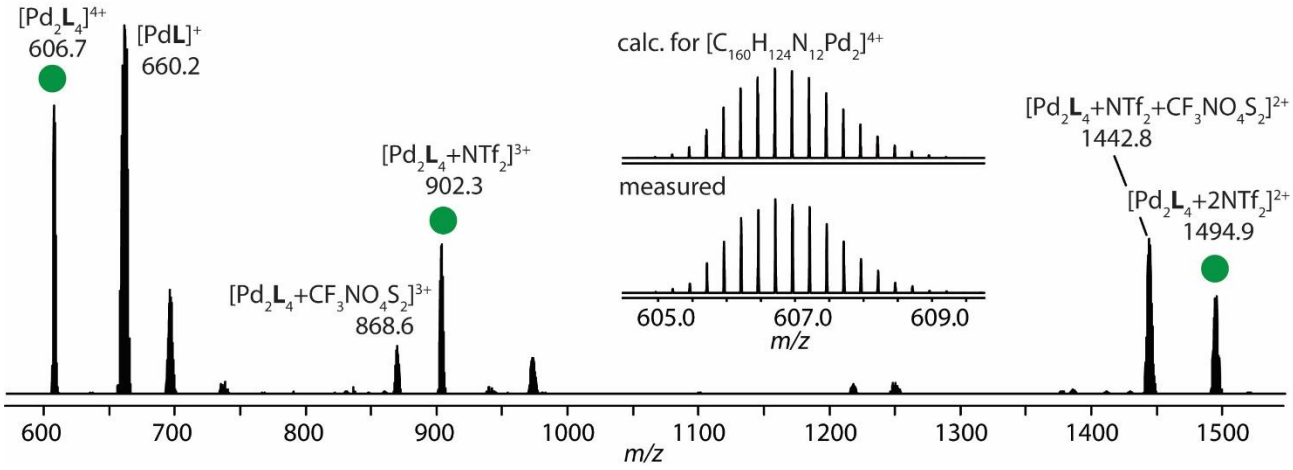

Figure S44. ESI-MS spectrum of the mixture of **1/1'**. The spectrum shows peaks of $[Pd_2\mathbf{L}_4](n NTf_2)^{4-n+}$ (n = 0–2) and the measured and calculated isotope pattern of $[Pd_2\mathbf{L}_4]^{4+}$ is also shown. Due to decomposition of the NTf_2 anion,[4] some peaks corresponding to $[Pd_2\mathbf{L}_4](nCF_3NO_4S_2)^{4-n+}$ (n = 1, 2) are present.

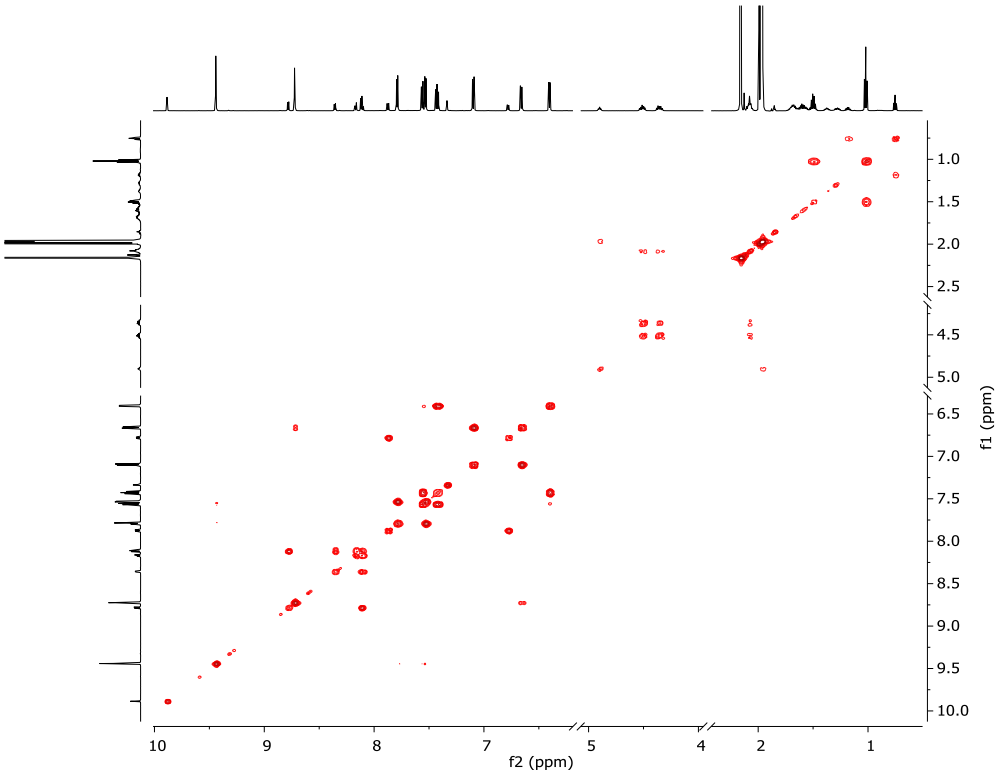

Figure S45. ^{1}H – ^{1}H COSY spectrum (600 MHz, CD_3CN) of the 4:1 mixture of **1/1'**.

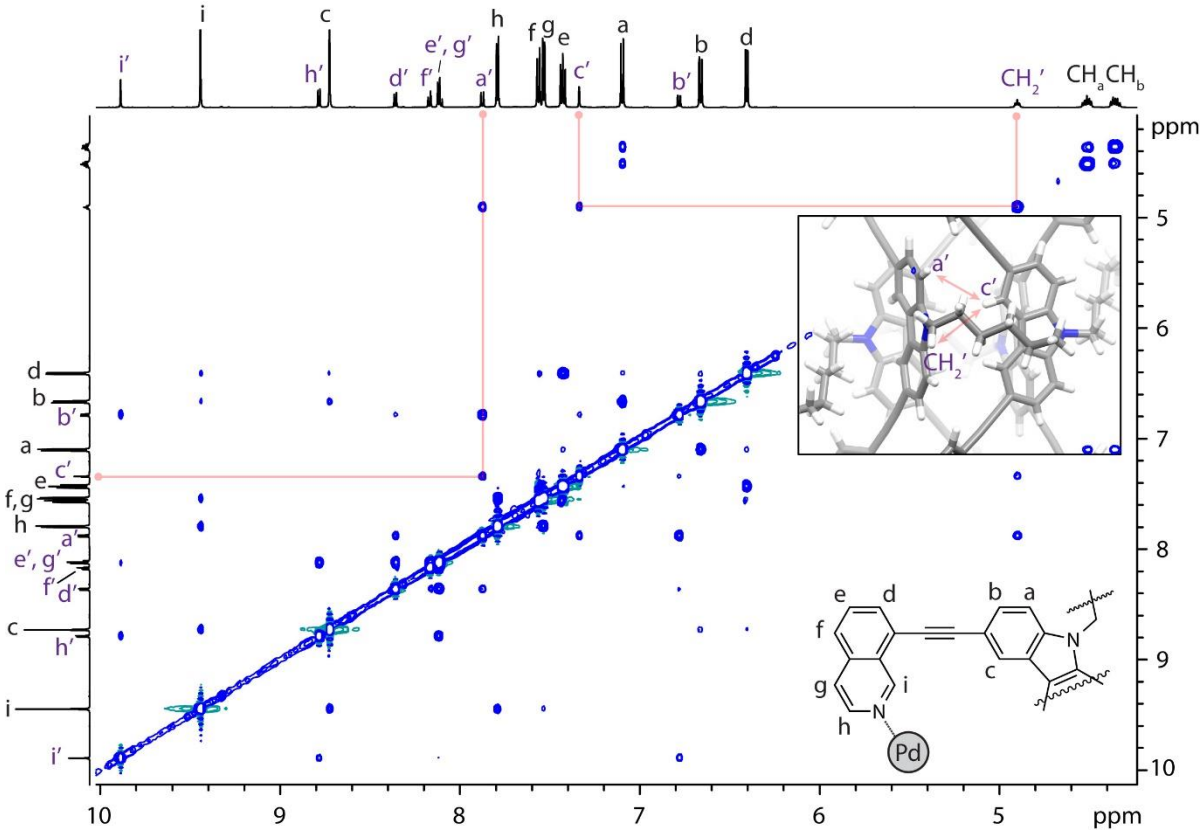

Figure S46. ^{1}H – ^{1}H NOESY spectrum (600 MHz, CD_3CN) of a 4:1 mixture of **1** and **1'**. The important NOE contacts of **1'** are highlighted and shown in the image of the crystal structure in the inset.

*1.3.9. Conversion of **1'** to **1·PF$_6$***

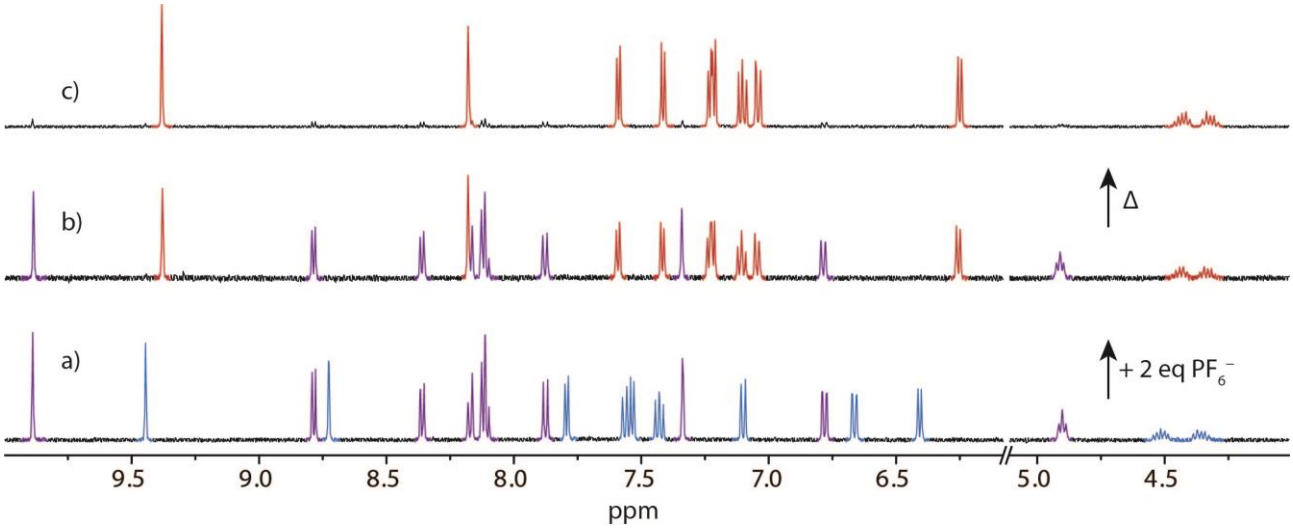

Figure S47. ^{1}H NMR spectra (500 MHz, CD_3CN) of a) an equilibrated 1:1 mixture of helicate **1** (blue) and mesocate **1'** (purple), obtained from the $[Pd(CH_3CN)](NTf)_2$ salt; b) the same sample with + 48µL (2 equivalents) of tetrabutylammonium hexafluorophosphate. The mixture was allowed to equilibrated over 24 h at room temperature. Red signals correspond to **1·PF$_6$**, ratio of **1'** to **1·PF$_6$**: 0.95:1.0 c) the same sample heated at 70°C for 24 h. As can be observed from the above spectra, the pre-organised and helical form **1** readily binds the PF_6^- guest at room temperature, although the conversion of the extended cage **1'** to **1·PF$_6$** requires additional energy (c).

1.3.10. Self-assembly of ***1·BF₄*** and ***1'*** in DMSO

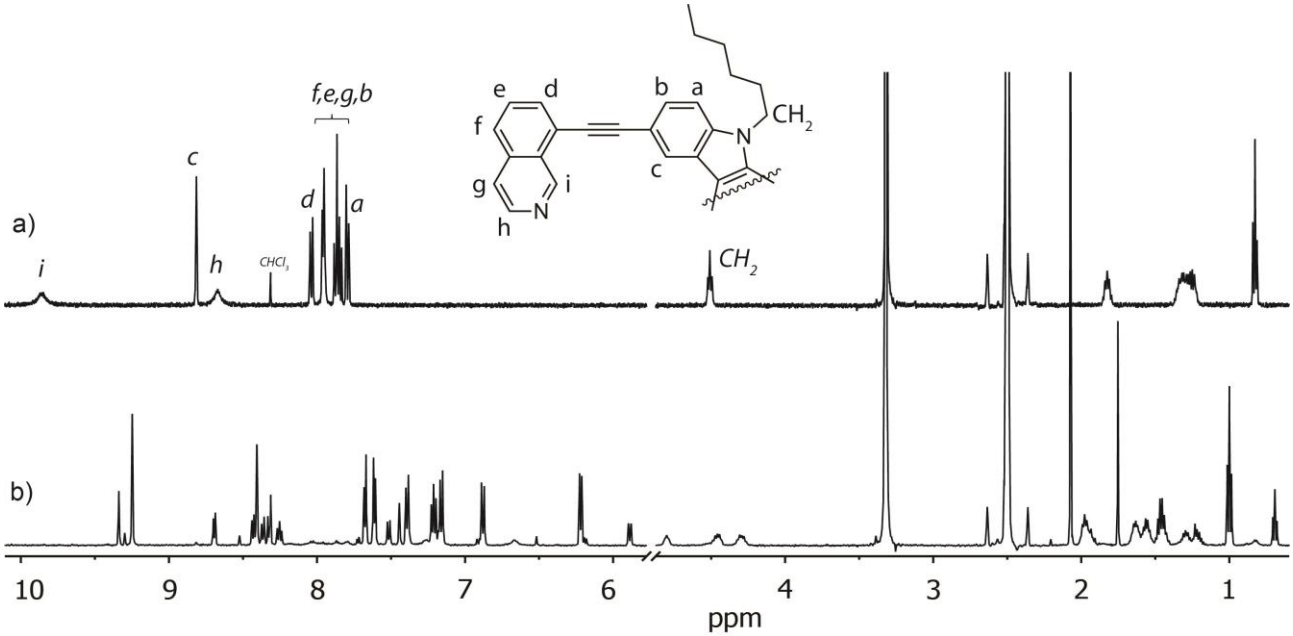

Figure S48. ^{1}H NMR spectra (500 MHz, DMSO-d_6): a) **L**; b) 2:1 mixture of $[Pd(CH_3CN)_4](BF_4)_2$ and **L**, heated at 70 °C for 1.5 h.

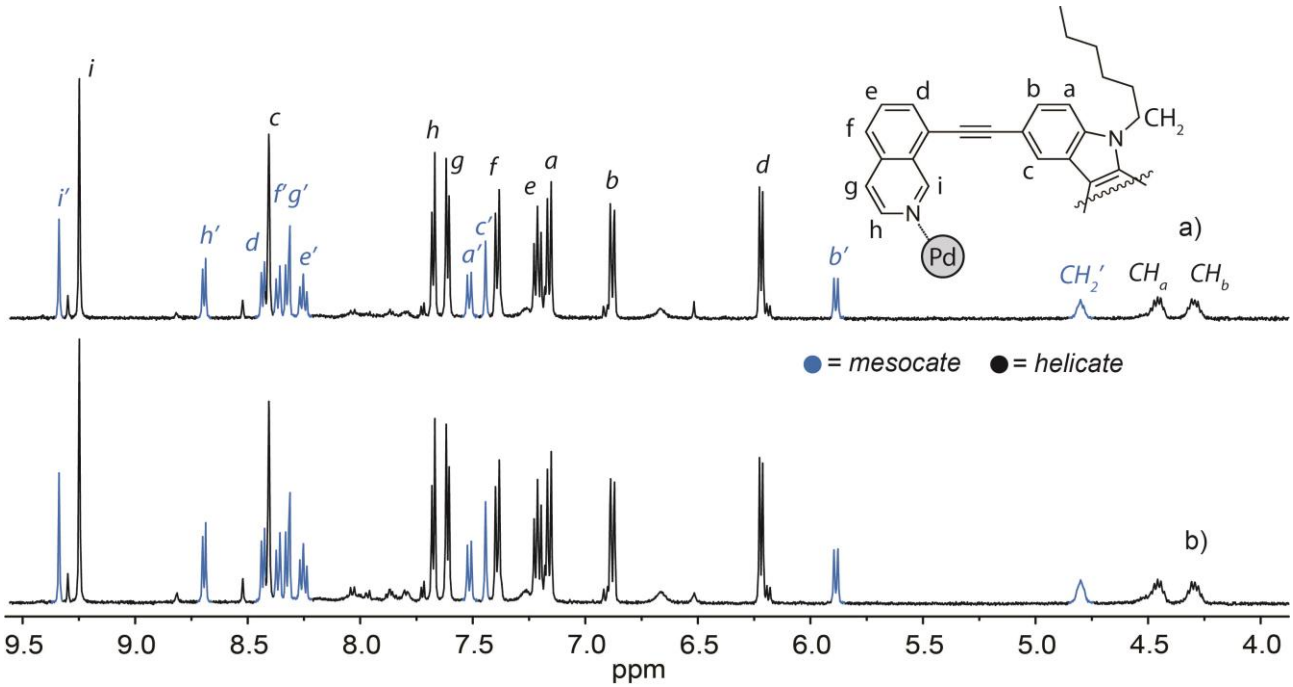

Figure S49. ^{1}H NMR spectra (500 MHz, DMSO-d_6): a) 2:1 mixture of $[Pd(CH_3CN)_4](BF_4)_2$ and **L**, heated at 70 °C for 1.5 h. Ratio of helicate to mesocate = 1:0.45; b) the same mixture after 24 h of heating at 70 °C. Ratio of helicate to mesocate = 1:0.52.

*1.3.11. Temperature equilibrium between **1·BF₄** and **1'** in CD_3CN*

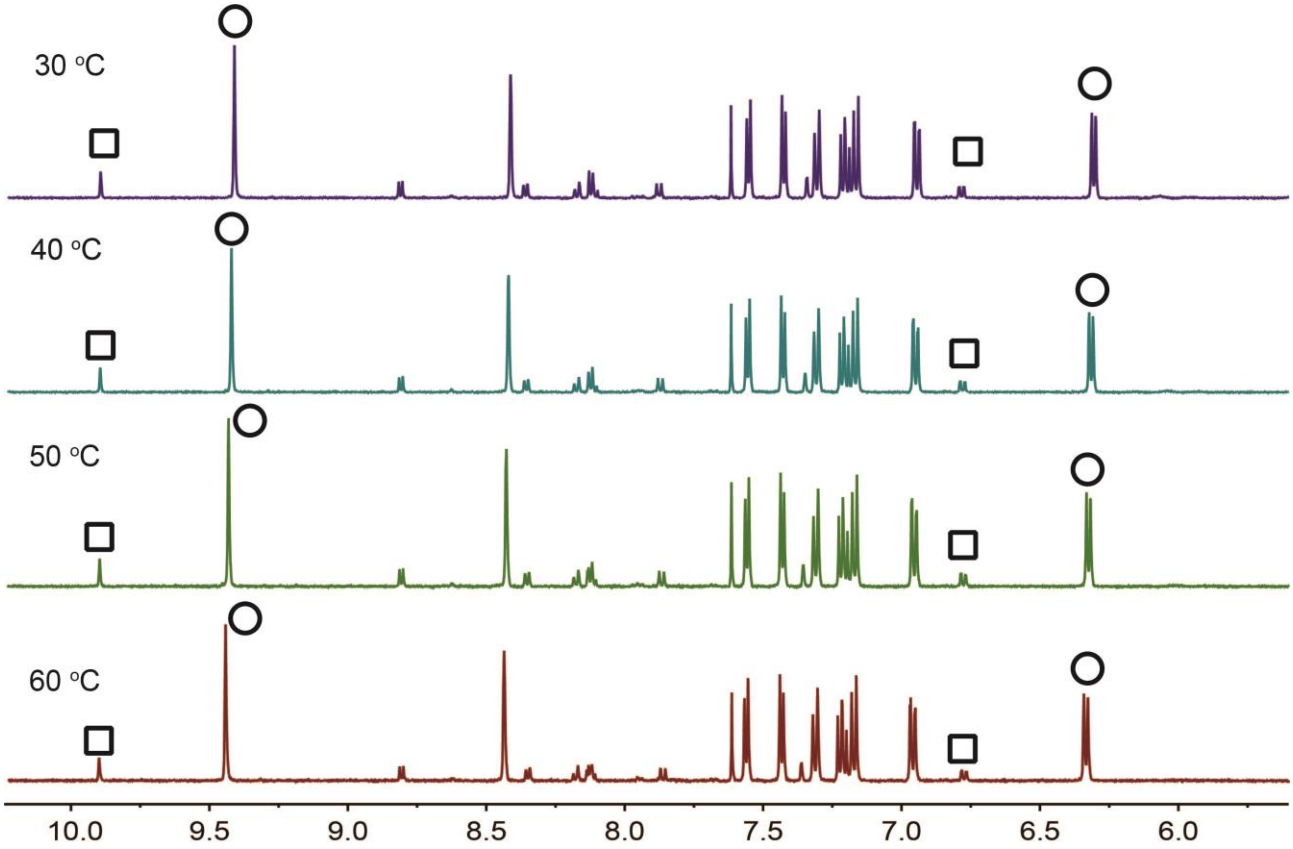

Figure S50. Variable temperature ^{1}H NMR spectra (500 MHz/CD_3CN) of **1·BF₄** (sample equilibrated over 3 months at room temperature). The peaks represented by the square (mesocate) and circle (helicate) were used calculate K.

Table 1.1 Calculated equilibrium between helicate **1·BF₄** and mesocate constant for various temperatures

T(K)	***K*** **(M^{-1})**	**lnK**
303.15	0.157031	-1.85131
313.15	0.152555	-1.88023
323.15	0.1467	-1.91936
333.15	0.130725	-2.03466

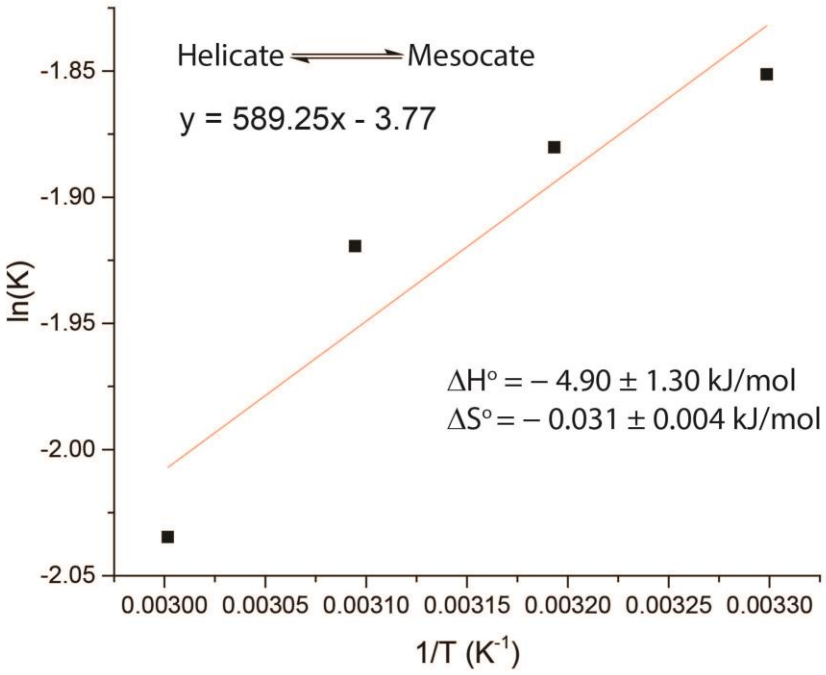

Figure S51. Van't hoff analysis of the equilibrium between helicate **1·BF$_4$** and mesocate **1'**. Standard errors of linear fit are given. The enthalpically driven isomerisation of the helicate may be driven by the relaxed ligand conformation and favourable edge-to-face π interactions present in the mesocate isomer, as compared to the strained, helical conformation of the ligand in the helicate isomer. This is counterbalanced by the enthalpically driven encapsulation of the anion, which is the driving force for the helicate as the only detectable product for **1·X** (X = ClO_4^-, PF_6^-, SbF_6^-, OTf^-)

2. ITC measurements

Table S3.1: Experiment and thermodynamic parameters of **1·NO$_3$** with X^- (X = BF_4^-, ClO_4^- and PF_6^-) measured by ITC

[a]*Anion*	*T (°C)*	*[Syr] (M)*	*[Cell] (M)*	*N (sites)*	*K_D (M)*	*K_D Error*	*ΔH (kcal/mol)*	*ΔH Error (kcal/mol)*	*ΔG (kcal/mol)*	*-TΔS (kcal/mol)*
BF_4^-	25.2	1.50E-02	2.50E-04	1	5.23E-04	2.29E-05	-0.875	2.10E-02	-4.48	-3.6
ClO_4^-	25.2	2.50E-03	2.50E-04	0.967	1.09E-05	3.07E-07	-3.81	2.20E-02	-6.77	-2.97
ReO_4^-	25.2	2.50E-03	2.50E-04	1	9.00E-07	7.92E-08	-5.87	4.40E-02	-8.25	-2.38

[a] Anions (as their tetrabutylammonium salts) were titrated into a freshly prepared solution of **1·NO$_3$** in CH_3CN. Note: the reference cell contained CH_3CN (HPLC grade).

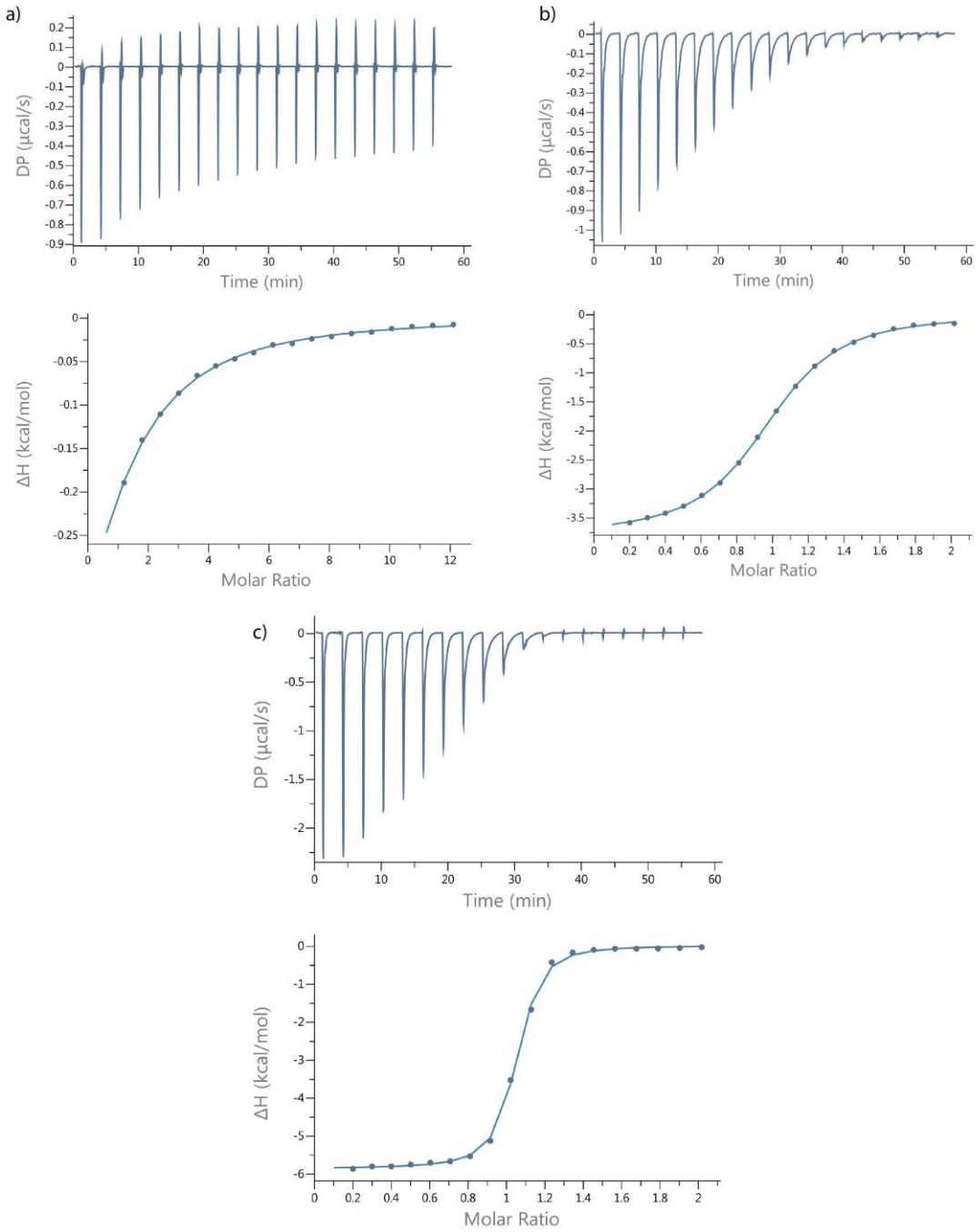

Figure S52. ITC analysis of the anion exchange of **1·NO_3** with X^-, where X = BF_4^- (a), ClO_4^- (b) and ReO_4^- (c). The upper graph is the raw ITC data for 19 automatic injections of the anion (guest) to the cage (host). The lower plot is the binding isotherm and cumulative heat of the injectant vs molar ratio of guest to host.

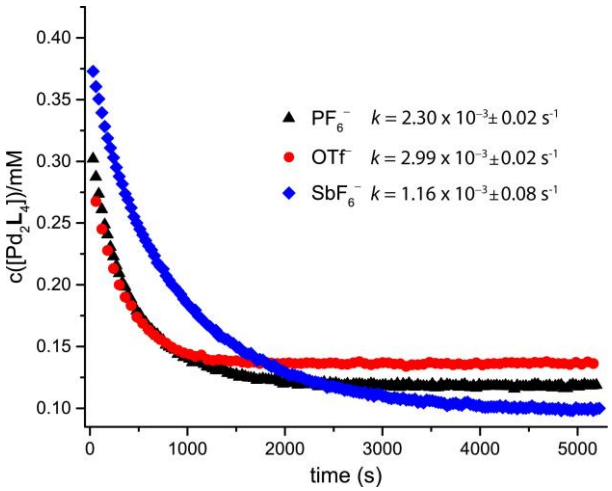

Figure S53. Kinetic data for the bimolecular process of anion exchange of **1·NO$_3$** with either PF_6^-, SbF_6^- or OTf^-. The data was obtained from time-resolved ^{1}H NMR spectra where 1 equivalent (24 µL) of a tetrabutylammonium salt of the guest was added to a solution of **1·NO$_3$** in CD_3CN (0.7 mM) at room temperature.

3. X-ray crystallography

Table 4.1: X-ray data of **1'**, **1·BF$_4$**, **1·ClO$_4$** and **1·PF$_6$**

Compound	**1'**	**1·BF$_4$**	**1·ClO$_4$**	**1·PF$_6$**
CCDC number	1851098	1851099	1851100	1851102
Empirical formula	$C_{164}H_{130}N_{19}O_{15}Pd_2$	$C_{160}H_{124}B_4F_{16}N_{12}Pd_2$	$C_{161}H_{124.5}Cl_{2.5}N_{13.5}O_{13}Pd_2$	$C_{166}H_{138}F_{24}N_{12}OP_4Pd_2$
Formula weight	2819.66	2774.74	2757.66	3109.56
Temperature (K)	80(2)	100(2)	100(2)	80(2)
Crystal system	Orthorhombic	Tetragonal	Tetragonal	Monoclinic
Space group	*Pccn*	*P4$_2$bc*	*P4$_2$bc*	*P2$_1$/n*
a (Å)	18.202(4)	30.0828(8)	30.020(4)	21.804(4)
b (Å)	29.004(6)	30.0828(8)	30.020(4)	25.207(5)
c (Å)	29.977(6)	29.4215(7)	29.369(6)	28.839(6)
α (º)	90	90	90	90
β (º)	90	90	90	97.68(3)
γ (º)	90	90	90	90
Volume (Å^3)	15826(5)	26625.7(16)	26467(9)	15708(6)
Z	4	8	8	4
Density (calc.) (Mg/m^3)	1.183	1.384	1.384	1.315
Absorption coefficient (mm^{-1})	0.162	2.857	3.229	0.193
F(000)	5836	11392	11388	6376
Crystal size (mm^3)	0.100x0.100x0.020	0.200x0.100x0.100	0.200x0.100x0.100	0.200x0.100x0.050
θ range for data collection (º)	1.077 to 20.200	2.077 to 78.590	2.081 to 44.564	0.854 to 19.964
Reflections collected	197129	149250	108011	183794
Observed reflections [R(int)]	15064 [0.0496]	26940 [0.0353]	10378 [0.0790]	28181 [0.0366]
Goodness-of-fit on F^2	1.462	1.102	1.012	1.031
R_1 [I>2σ(I)]	0.1170	0.0875	0.0891	0.0911
wR_2 (all data)	0.4027	0.2674	0.2527	0.2823
Largest diff. peak and hole (e.Å-3)	1.896 and -0.882	4.033 and -1.088	0.844 and -0.631	1.326 and -1.055
Data / restraints / parameters	15064 / 2084 / 1048	26940 / 2348 / 1898	10378 / 2348 / 1877	28181 / 4415 / 2010

Table 4.2: X-ray data of **1·ReO_4**, **1·SbF_6** and **1·OTf**

Compound	**1·ReO_4**	**1·SbF6**	**1·OTf**
CCDC number	1851101	1851103	1851104
Empirical formula	$C_{160}H_{124}N_{13}O_{11}Pd_2Re_2$	$C_{169}H_{145}F_{24}N_{12}O_{1.5}Pd_2Sb_4$	$C_{171.25}H_{142}F_{10.5}N_{12}O_{11.75}Pd_2S_{3.5}$
Formula weight	2989.91	3523.76	3080.47
Temperature (K)	100(2)	80(2)	80(2)
Crystal system	Tetragonal	Monoclinic	Monoclinic
Space group	*P*4_2*bc*	*P*2_1/*n*	*P*2_1/*n*
a (Å)	30.0723(9)	22.378(5)	17.107(3)
b (Å)	30.0723(9)	25.420(5)	33.911(7)
c (Å)	29.2855(18)	29.183(6)	27.153(5)
α (º)	90	90	90
β (º)	90	97.42(3)	99.19(3)
γ (º)	90	90	90
Volume (Å^3)	26484(2)	16462(6)	15550(6)
Z	8	4	4
Density (calc.) (Mg/m^3)	1.500	1.422	1.316
Absorption coefficient (mm^{-1})	2.140	0.504	0.194
F(000)	12040	7068	6360
Crystal size (mm^3)	0.200x0.200x0.200	0.080x0.080x0.030	0.100x0.050x0.010
θ range for data collection (º)	1.391 to 26.816	0.845 to 21.973	0.768 to 21.964
Reflections collected	133584	265657	251043
Observed reflections [R(int)]	27659 [0.0402]	40225 [0.0389]	37560 [0.0406]
Goodness-of-fit on F^2	1.051	1.061	1.022
R_1 [I>2σ(I)]	0.1069	0.0721	0.0945
wR_2 (all data)	0.3144	0.2326	0.3076
Largest diff. peak and hole (e.Å-3)	2.369 and -4.030	1.969 and -2.312	2.177and -1.728
Data / restraints / parameters	27659 / 3570 / 1741	40225 / 4815 / 2196	37560 / 2576/ 2139

4.1. General details

1·BF_4, **1·ClO_4**: A single crystal in mother liquor was pipetted onto a glass slide containing NVH oil. The crystal was quickly mounted onto a 0.2 mm nylon loop and measured on a Bruker D8 venture equipped with an Incoatec microfocus source (Iμs 2.0) using Cuk_α radiation.

1', **1·PF_6**, **1·SbF_6**, **1·OTf:** A single crystal in mother liquor was pipetted onto a glass slide, mounted onto a 0.2 mm or 0.3 mm loop and placed in UNI Pucks at cryogenic temperatures. The UNI Pucks were placed in a dry shipper which enabled safe transportation to the macromolecular beamline P11[5] at Petra III, DESY, Germany. UNI Pucks were transferred to the sample dewar and all samples were mounted using the StäubliTX60L robotic arm. A wavelength of 0.6889 Å was chosen using a liquid N_2 cooled double crystal monochromator. Single crystal X-ray diffraction data was collected at 80(2) K on a single axis goniometer, equipped with an Oxford Cryostream 800 a Pilatus 6M fast.

The structures were solved by intrinsic phasing/direct methods using SHELXT[6] and refined with SHELXL[7] using 22 cpu cores for full-matrix least-squares routines on F^2 and ShelXle[8] as a graphical user interface and the DSR program plugin was employed for modelling.[9]

Stereochemical restraints for the CHQ ligands, solvent molecules and counter ions of the structure were generated by the GRADE program using the GRADE Web Server (http://grade.globalphasing.org) and applied in the refinement. A GRADE dictionary for SHELXL contains target values and standard deviations for 1,2-distances (DFIX) and 1,3-distances (DANG), as well as restraints for planar groups (FLAT). All displacements

for non-hydrogen atoms were refined anisotropically. The refinement of ADP's for carbon, nitrogen and oxygen atoms was enabled by a combination of similarity restraints (SIMU) and rigid bond restraints (RIGU).[10] The contribution of the electron density from disordered counterions and solvent molecules, which could not be modelled with discrete atomic positions were handled using the SQUEEZE[11] routine in PLATON[12]. The solvent mask file (.fab) computed by PLATON were included in the SHELXL refinement via the ABIN instruction leaving the measured intensities untouched.

4.2. Specific details

*4.2.1. Specific details on **1'***

This structure was treated with SQUEEZE protocol inside PLATON because the crystal lattice contains large voids filled with scattered electron density derived from the disordered solvent molecules. One hexyl chain on the CHQ ligand was solved as a conformational disordered model at two positions, whose occupancies were 0.62 and 0.38, respectively. Three NO_3 anions were located at special positions, whose occupancies were treated as 0.5.

Ligand	Residue class	Occurrence	Residue numbers
Pd^{2+}	PD	2	9
CHQ	CHQ	4	1, 2
Acetonitrile	ACN	2	3
NO_3^-	NO3	5	4-8

*4.2.2. Specific details on **1·BF₄***

This structure was refined as two component twin using BASF/TWIN instructions, resulting in the BASF parameter of ~30% and a Flack parameter of 0.0222(18). The BF_4 anion trapped within the helical cage was disordered with three conformations which were refined isotropically and their occupancies were refined using SUMP instruction. Two hexyl chains on the CHQ ligands were solved as conformational disordered models at two positions.

Ligand	Residue class	Occurrence	Residue numbers
Pd^{2+}	PD	2	12
CHQ	CHQ	4	1, 2, 3, 4
BF_4^-	BF4	4	5–11

*4.2.3. Specific details on **1·ClO₄***

This structure was refined as two component twin using BASF/TWIN instructions, resulting in the BASF parameter of ~25% and a Flack parameter of –0.013(4). The ClO_4 anion trapped within the helical cage was disordered with two conformations whose occupancies were 0.63 and 0.37, respectively. Owing to the poor scattering power of the crystal, all of the counter anions were not refined. Some NO_3 anions could be refined, which were consistent with ESI-MS analysis (Figure S18).

Ligand	Residue class	Occurrence	Residue numbers
Pd^{2+}	PD	2	11
CHQ	CHQ	4	1, 2, 3, 4
Acetonitrile	ACN	0.5	10
ClO_4^-	CLO	2.5	5, 6, 7
NO_3^-	NO3	1	8, 9

*4.2.4. Specific details on **1·PF_6***

This structure was treated with SQUEEZE protocol inside PLATON because the crystal lattice contains large voids filled with scattered electron density derived from the disordered solvent molecules. The PF_6 anion trapped within the helical cage was disordered with two conformations whose occupancies were 0.48 and 0.52, respectively. One PF_6 anion located at the outside of the cage was treated as a disordered model.

Ligand	Residue class	Occurrence	Residue numbers
Pd^{2+}	PD	2	12
CHQ	CHQ	4	1, 2, 3, 4
PF_6^-	PF6	4	5-10
Diisopropylether	DIP	1	11

*4.2.5. Specific details on **1·ReO_4***

This structure was treated with SQUEEZE protocol inside PLATON because the crystal lattice contains large voids filled with scattered electron density derived from the disordered solvent molecules. This structure was also refined as two component twin using BASF/TWIN instructions, resulting in the BASF parameter of ~43% and a Flack parameter of –0.002(3). The ReO_4 anion trapped within the helical cage was disordered with two conformations whose occupancies were 0.53 and 0.47, respectively. Owing to the poor scattering power of the crystal, all of the counter anions were not refined. One NO_3 anion could be observed in this refinement, which was consistent with ESI-MS measurement (Figure S41).

Ligand	Residue class	Occurrence	Residue numbers
Pd^{2+}	PD	2	13
CHQ	CHQ	4	1, 2, 3, 4
ReO_4^-	REO4	2	5, 6, 7
NO_3^-	NO3	1	9

*4.2.6. Specific details on **1·SbF_6***

This structure was treated with SQUEEZE protocol inside PLATON because the crystal lattice contains large voids filled with scattered electron density derived from the disordered solvent molecules. The SbF_6 anion trapped within the helical cage was disordered with two conformations whose occupancies were 0.57 and 0.43, respectively. Two PF_6 anions located at the outside of the cage were disordered at two positions. Two hexyl chains on the CHQ ligands were solved as conformational disordered models.

Ligand	Residue class	Occurrence	Residue numbers
Pd^{2+}	PD	2	19
CHQ	CHQ	4	1, 2, 3, 4
SbF_6^-	SBF	4	5–11
Diisopropylether	DIP	1.5	13, 14

*4.2.7. Specific details on **1·OTf***

This structure was treated with SQUEEZE protocol inside PLATON because the crystal lattice contains large voids filled with scattered electron density derived from the disordered solvent molecules. The OTf anion trapped within the helical cage was disordered with two conformations whose occupancies were 0.63 and 0.37, respectively. The occupancy of one OTf anion located at the outside of the cage was refined as 0.5 due to its extremely high flexibility. Two hexyl chains on the CHQ ligands were solved as conformational disordered models.

Ligand	Residue class	Occurrence	Residue numbers
Pd^{2+}	PD	2	16
CHQ	CHQ	4	1, 2, 3, 4
OTf^-	TFA	3.5	5–9
Diisopropylether	DIP	1.5	11, 12

4.3. Thermal ellipsoid plots

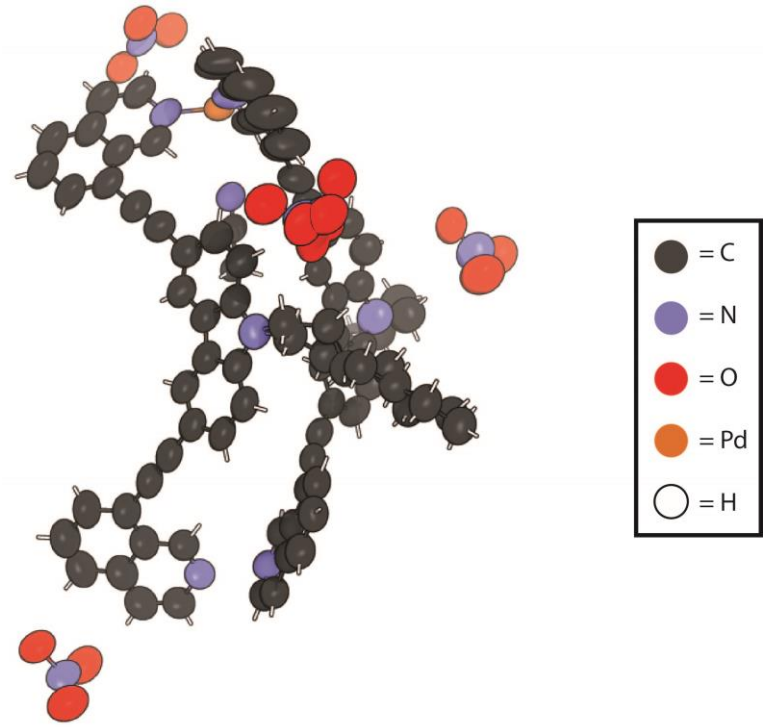

Figure S54. The asymmetric unit of **1'** (obtained from the solution of **1·NO_3**) with all non-hydrogen atoms shown as ellipsoids at the 50% probability level.

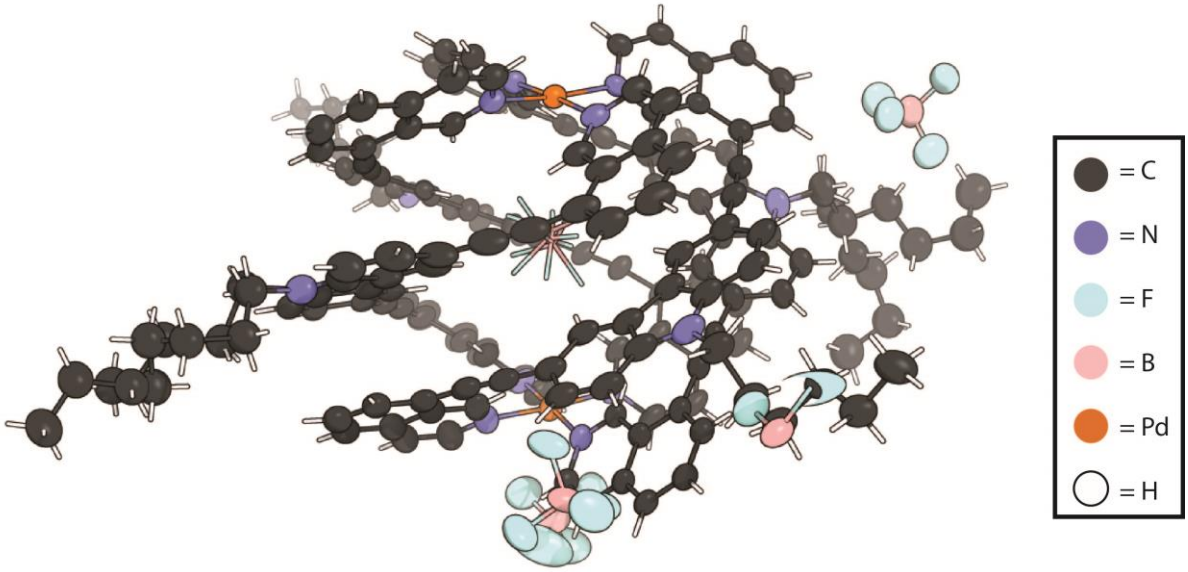

Figure S55. The asymmetric unit of **1·BF_4** with all non-hydrogen atoms shown as ellipsoids at the 50% probability level (exception: encapsulated BF_4^- guests).

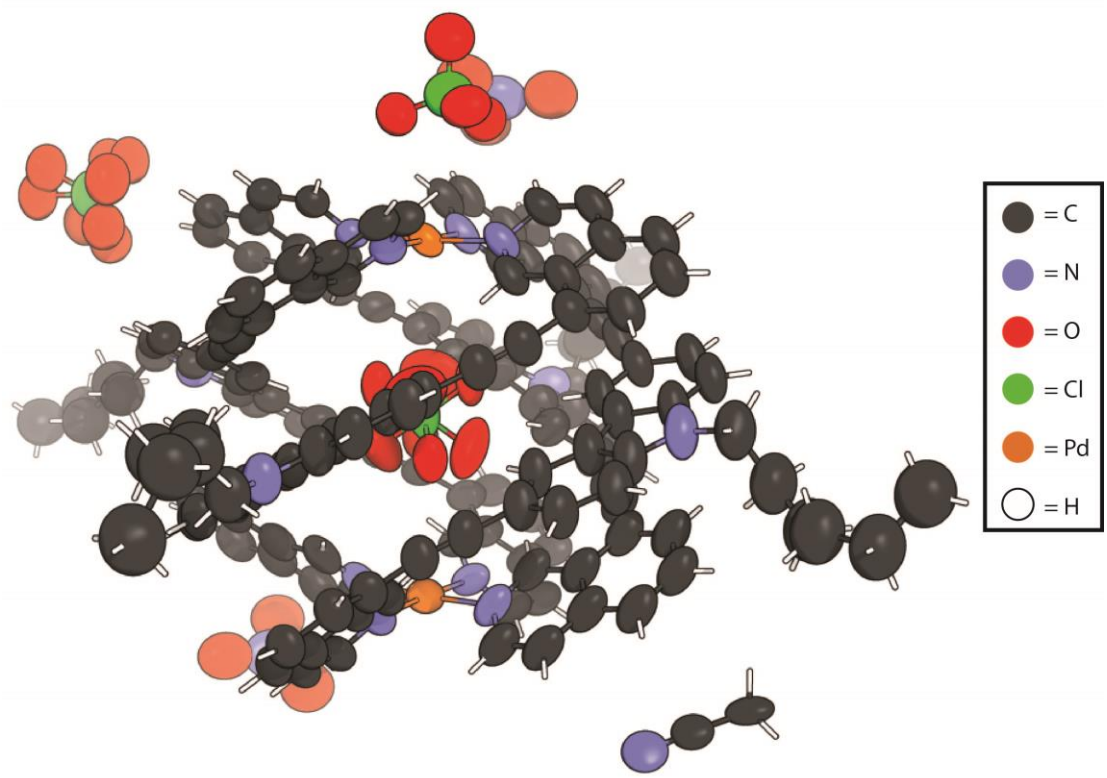

Figure S56. The asymmetric unit of **1·ClO$_4$** with all non-hydrogen atoms shown as ellipsoids at the 50% probability level.

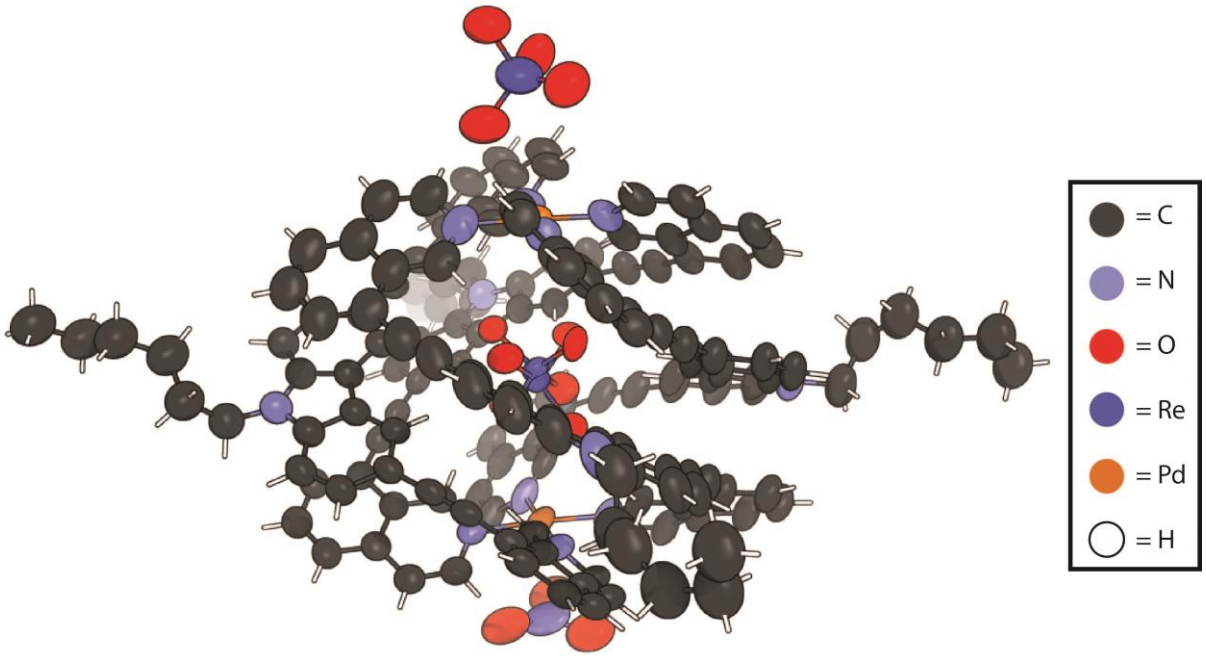

Figure S57. The asymmetric unit of **1·ReO$_4$** with all non-hydrogen atoms shown as ellipsoids at the 50% probability level.

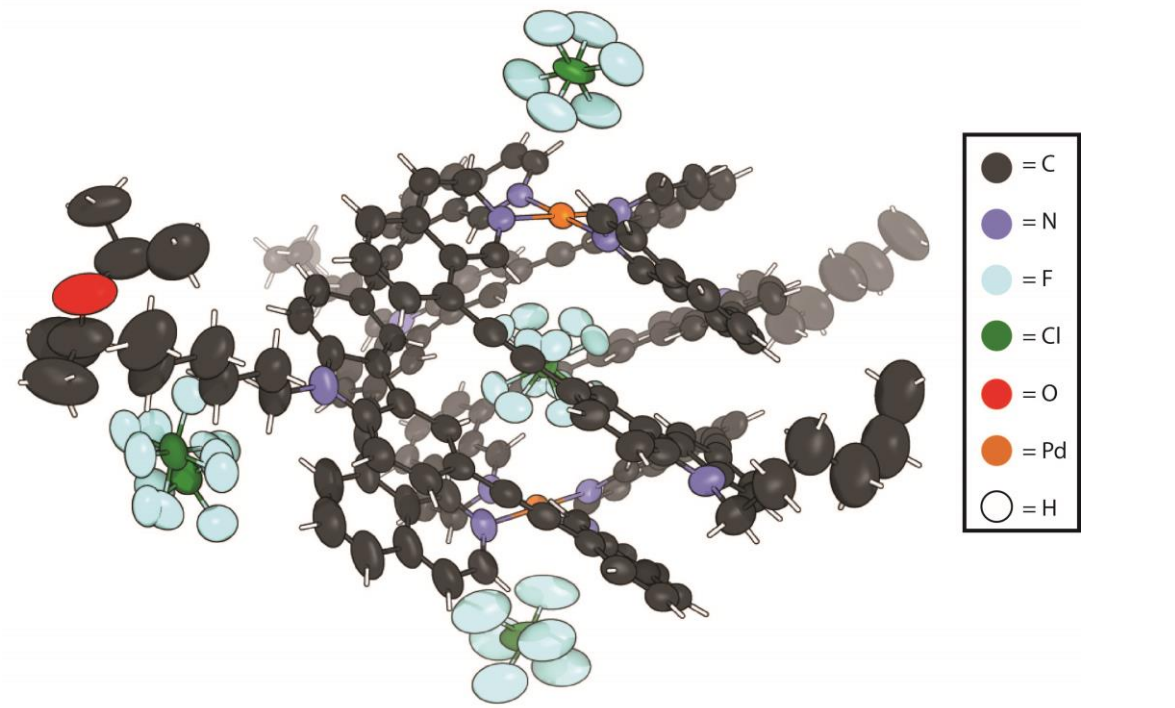

Figure S58. The asymmetric unit of **1·PF_6** with all non-hydrogen atoms shown as ellipsoids at the 50% probability level.

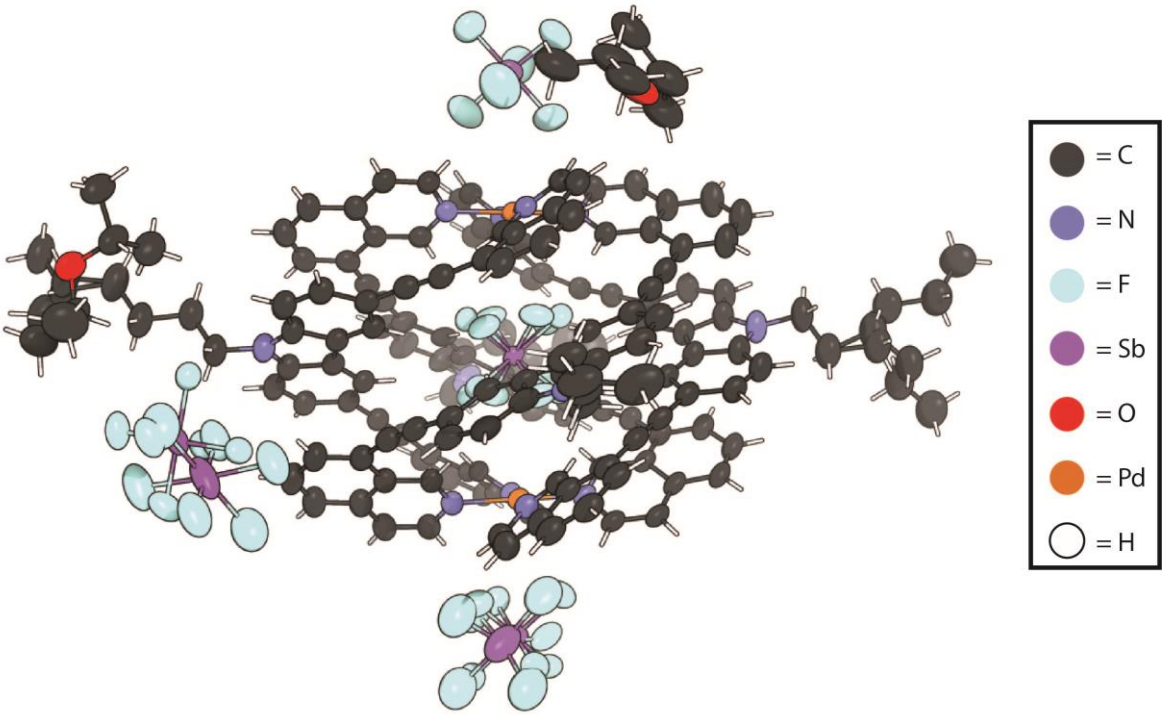

Figure S59. The asymmetric unit of **1·SbF_6** with all non-hydrogen atoms shown as ellipsoids at the 50% probability level.

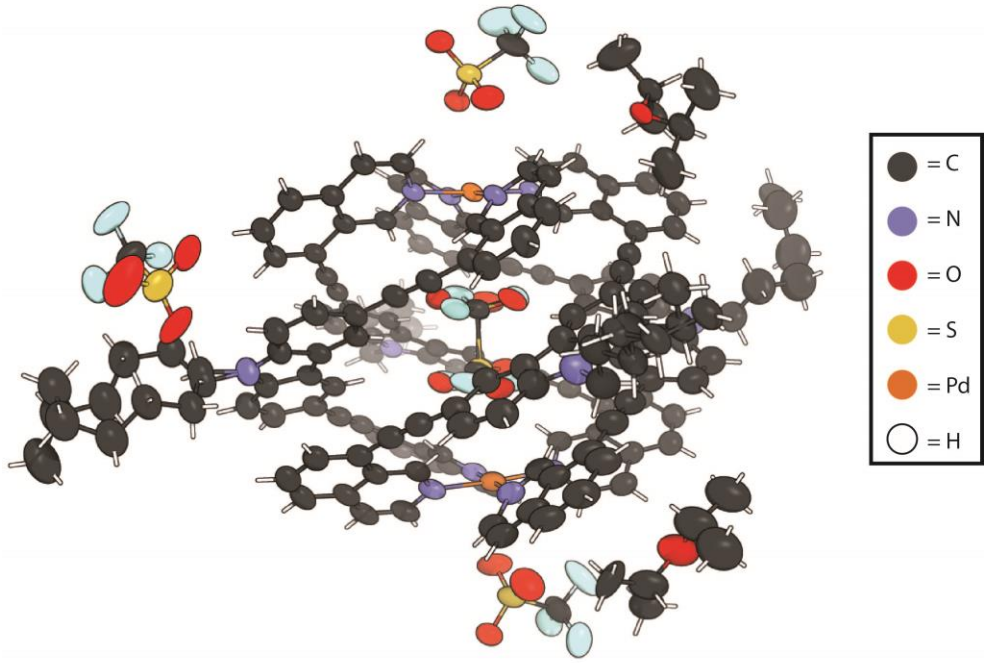

Figure S60. The asymmetric unit of **1·OTf** with all non-hydrogen atoms shown as ellipsoids at the 50% probability level.

4.4. Solid-state structural metrics of 1

Table 4.3: Solid-state structural parameters of **1·X**.

Sample	Pd···Pd distance (Å)	Anion volume (Å^3)[a]	Cavity volume (Å^3)[b]	Packing coefficient	Twist angle (°)[c]
1·BF_4	9.287	54.85	119.13	0.460	171.6
1·ClO_4	9.040	55.44	123.87	0.447	171.2
1·ReO_4	8.990	59.10	127.37	0.464	172.5
1·PF_6	8.713	74.88	128.40	0.583	174.3
1·SbF_6	8.805	84.85	140.67	0.603	176.2
1·OTf	9.400	85.37	137.29	0.622	174.8

[a]Calculated by DFT geometry optimization (R3BLYP; B, O, F, Cl, P, S: 6-31g(d); Re, Sb: LANL2DZ)
[b]Calculated using VOIDOO (1.4 Å probe radius)
[c]Averaged value of plane angles between N4–Pd1–Pd2 and N31–Pd2–Pd1 planes determined by the MPLA command in SHELXL-2014/7. The same values can be obtained by measuring and averaging torsion angles of N4–Pd1–Pd2–N31.

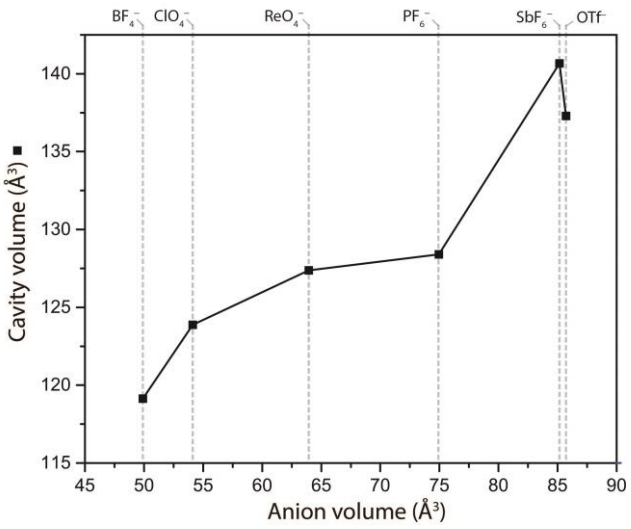

Figure S61. A graph showing the relationship between the anion volume and the cavity volume of **1·X**. The data plotted was obtained from the X-ray crystal structures.

5. Ion-Mobility Mass Spectrometry

Ion mobility measurements were performed on a Bruker timesTOF instrument combining a trapped ion mobility (TIMS) with a time-of-flight (TOF) mass spectrometer in one instrument. In contrast to the conventional drift tube method to determine mobility data, where ions are carried by an electric field through a stationary drift gas, the TIMS method is based on an electric field ramp to hold ions in place against a carrier gas pushing them in the direction of the analyzer. Consequently, larger sized ions that experience more carrier gas impacts leave the TIMS units first and smaller ions elute later. This method offers a much higher mobility resolution despite a smaller device size.

5.1. Sample preparation

1·NO$_3$, **1·BF$_4$**, **1·ClO$_4$**, **1·SbF$_6$**, **1·OTf**, **1·NTf$_2$** (**1/1'**): The measurement samples (10 µM CH_3CN solution) were prepared by dilution of $[Pd_2\mathbf{L}_4](X)_4$ solutions (2.2 mM) obtained according to the general procedure.

1·ReO$_4$, **1·PF$_6$**: The measurement samples (10 µM CH_3CN solution) were prepared by a dilution of mixtures of $[Pd_2\mathbf{L}_4](NO_3)_4$ (2.2 mM) and tetrabutyl ammounim salts ($[^nBu_4N][ReO_4]$ or $[^nBu_4N][PF_6]$) (8.8 mM).

5.2. Measurement conditions

After the generation of ions by electrospray ionisation (ESI, sample concentration: 10 µM, solvent CH_3CN, capillary voltage: 3600 V, end plate offset voltage: 500 V, nebulizer gas pressure: 0.3 bar, dry gas flow rate: 3.5 l/min, dry temperature 200 ºC) the desired ions were orthogonally deflected into the TIMS cell consisting of an entrance funnel, the TIMS analyser (carrier gas: N2, temperature: 305 K, entrance pressure: 2.55 mbar, exit pressure: 0.89 mbar, IMS imeX ramp end 1.88 1/K0, IMS imeX ramp start: 0.77 1/K0). As a result, the ions are stationary trapped. After accumulation (accumulation time: 5 ms), a stepwise reduction of the electric field strength leads to a release of ion packages separated by their mobility. After a subsequent focussing, the separated ions are transferred to the TOF-analyser.[13–15] For calibration of both the TIMS and TOF analysers, commercially available Agilent ESI tuning mix was used. The instrument was calibrated before each measurement, including each change in the ion mobility resolution mode ("imeX" settings: survey, detect or ultra).

5.3. Ion-Mobility data of $[(Pd_2L_4)(X)]^{3+}$ and $[(Pd_2L_4)(X_2)]^{2+}$

*5.3.1. Ion-Mobility spectra of **1·NO$_3$**: $[(Pd_2\mathbf{L}_4)(NO_3)]^{3+}$ and $[(Pd_2\mathbf{L}_4)(NO_3)_2]^{2+}$.*

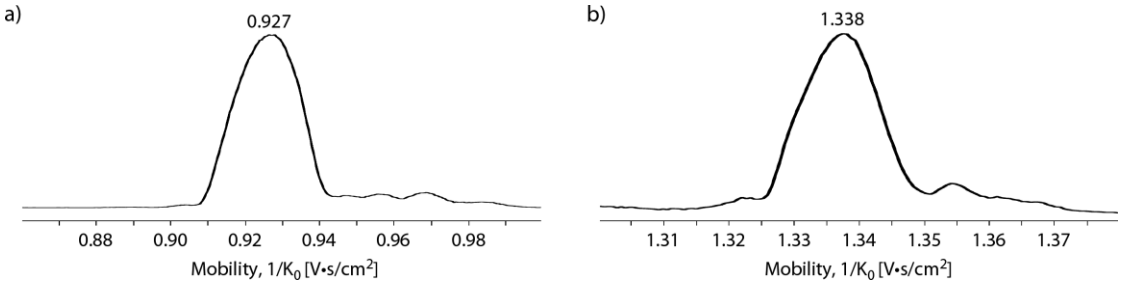

Figure S62. Extracted ion mobilograms of (a) $[(Pd_2\mathbf{L}_4)(NO_3)]^{3+}$ at *m/z* 829.6 and (b) $[(Pd_2\mathbf{L}_4)(NO_3)_2]^{2+}$ at *m/z* 1275.4.

*5.3.2. Ion-Mobility spectra of **1·BF$_4$**: $[(Pd_2\mathbf{L}_4)(BF_4)]^{3+}$ and $[(Pd_2\mathbf{L}_4)(BF_4)_2]^{2+}$.*

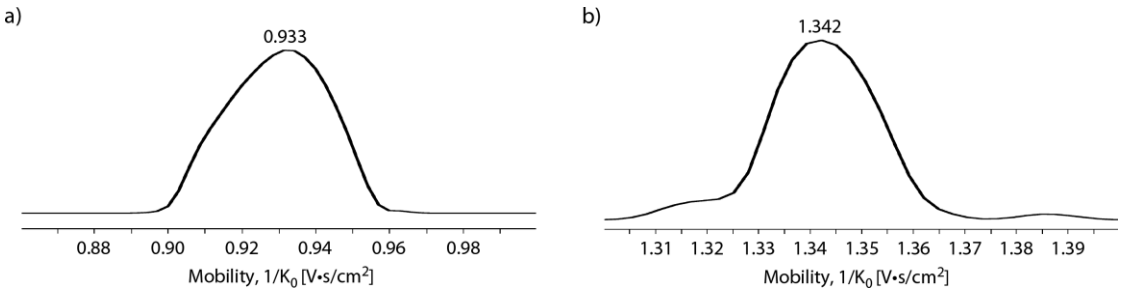

Figure S63. Extracted ion mobilograms of (a) $[(Pd_2\mathbf{L}_4)(BF_4)]^{3+}$ at *m/z* 837.9 and (b) $[(Pd_2\mathbf{L}_4)(BF_4)_2]^{2+}$ at *m/z* 1300.4.

*5.3.3. Ion-Mobility spectra of **1·ClO₄**: $[(Pd_2L_4)(ClO_4)]^{3+}$ and $[(Pd_2L_4)(ClO_4)_2]^{2+}$.*

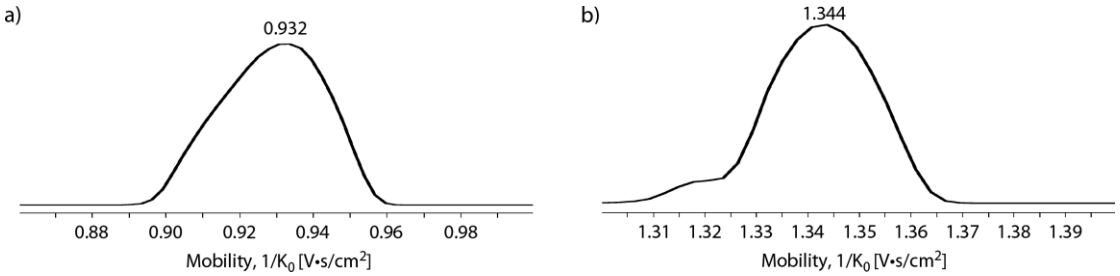

Figure S64. Extracted ion mobilograms of (a) $[(Pd_2L_4)(ClO_4)]^{3+}$ at *m/z* 842.3 and (b) $[(Pd_2L_4)(ClO_4)_2]^{2+}$ at *m/z* 1313.4.

*5.3.4. Ion-Mobility spectra of **1·ReO₄**: $[(Pd_2L_4)(ReO_4)]^{3+}$ and $[(Pd_2L_4)(ReO_4)_2]^{2+}$.*

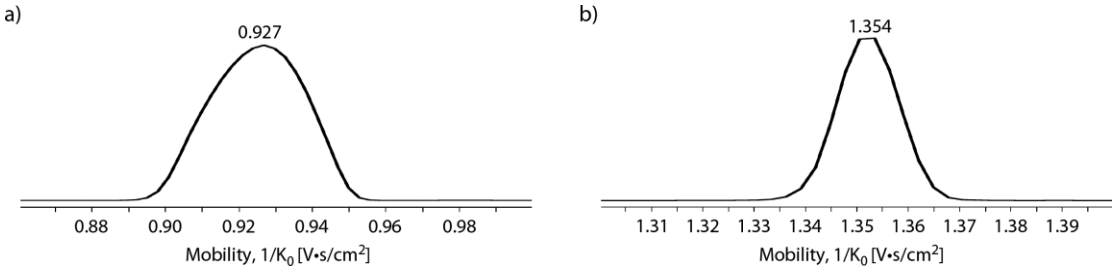

Figure S65. Extracted ion mobilograms of (a) $[(Pd_2L_4)(ReO_4)]^{3+}$ at *m/z* 892.6 and (b) $[(Pd_2L_4)(ReO_4)_2]^{2+}$ at *m/z* 1463.4.

*5.3.5. Ion-Mobility spectra of **1·PF₆**: $[(Pd_2L_4)(PF_6)]^{3+}$ and $[(Pd_2L_4)(PF_6)_2]^{2+}$.*

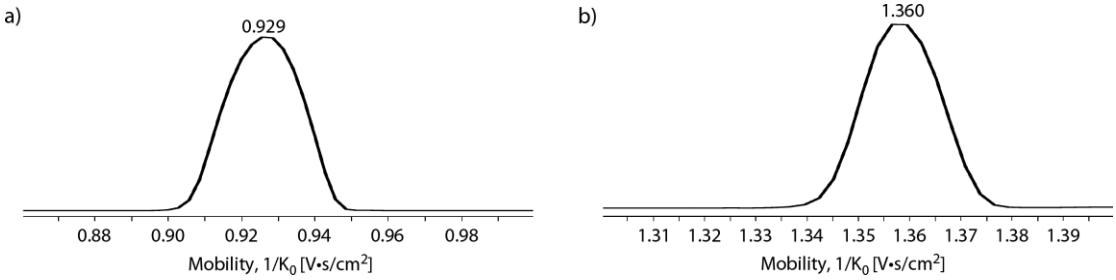

Figure S66. Extracted ion mobilograms of (a) $[(Pd_2L_4)(PF_6)]^{3+}$ at *m/z* 857.3 and (b) $[(Pd_2L_4)(PF_6)_2]^{2+}$ at *m/z* 1358.4.

*5.3.6. Ion-Mobility spectra of **1·SbF₆**: $[(Pd_2L_4)(SbF_6)]^{3+}$ and $[(Pd_2L_4)(SbF_6)_2]^{2+}$.*

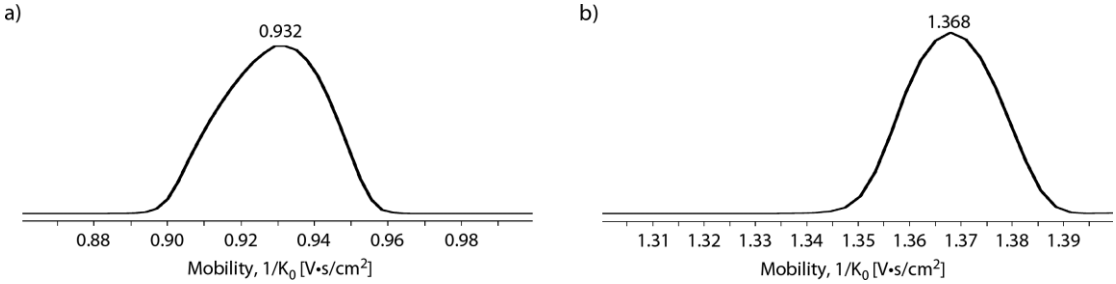

Figure S67. Extracted ion mobilograms of (a) $[(Pd_2L_4)(SbF_6)]^{3+}$ at *m/z* 887.6 and (b) $[(Pd_2L_4)(PF_6)_2]^{2+}$ at *m/z* 1449.3.

*5.3.7. Ion-Mobility spectra of **1·OTf**: $[(Pd_2L_4)(OTf)]^{3+}$ and $[(Pd_2L_4)(OTf)_2]^{2+}$.*

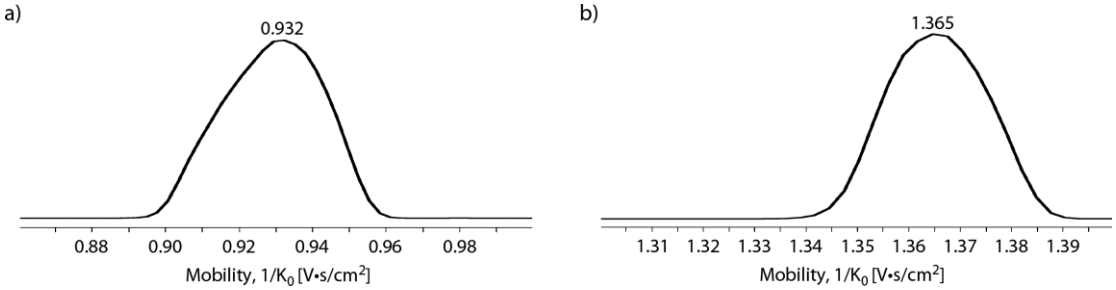

Figure S68. Extracted ion mobilograms of (a) $[(Pd_2L_4)(OTf)]^{3+}$ at *m/z* 858.6 and (b) $[(Pd_2L_4)(OTf)_2]^{2+}$ at *m/z* 1362.4.

Table S5.1: Experimental and theoretical collision cross sections of $[(Pd_2L_4)(X)]^{3+}$ and $[(Pd_2L_4)(X)_2]^{2+}$.[a]

Anion	*$[(Pd_2L_4)(X)]^{3+}$*				*$[(Pd_2L_4)(X)_2]^{2+}$*			
	Mobility ($1/K_0$)	CCS (exp) (Å^2)	CCS (calcd)[b] (Å^2)	CCS (calcd)[c] (Å^2)	Mobility ($1/K_0$)	CCS (exp) (Å^2)	CCS (calcd)[b] (Å^2)	CCS (calcd)[c] (Å^2)
NO_3^-	0.927(17)	560(10)	–	–	1.338(9)	539(4)	–	–
BF_4^-	0.933(30)	564(17)	580.7(36)	614.6(53)	1.342(20)	540(8)	590.1(49)	613.7(30)
ClO_4^-	0.932(29)	563(18)	580.7(36)	611.4(35)	1.344(20)	541(8)	586.9(44)	605.0(42)
ReO_4^-	0.927(26)	560(16)	573.1(43)	610.3(46)	1.354(14)	545(5)	589.6(36)	614.2(57)
PF_6^-	0.929(24)	561(13)	563.8(62)	599.9(51)	1.360(17)	547(7)	583.4(44)	603.7(45)
SbF_6^-	0.932(28)	562(17)	562.8(34)	599.5(29)	1.368(19)	551(8)	580.6(26)	606.4(51)
OTf^-	0.932(24)	563(17)	568.6(48)	606.9(36)	1.365(23)	549(9)	590.8(32)	610.7(61)

[a] Measured at 305 K in N_2 drift gas. [b, c] Obtained from the X-ray crystal structures deduced computationally using the trajectory (TJ) method of the N2_MOBCAL program (b) without and (c) with partial charges on each atom. The partial charges were obtained single-point calculations with DFT method using B3LYP function. LanL2DZ and 6-31G(d,p) were employed to treat Pd, Re, Sb and other atoms, respectively. The numbers in parentheses are the corresponding standard deviations.

We also examined the 2+ species (**1·X$_2$**) to investigate the effect that the additional, non-encapsulated anion has on their size. CCS calculations revealed that the 2+ species gradually become larger as the size of the anion increases. This trend explains the structural preferences of **1·X$_2$**, whose two anions are located inside the helical cage and above the Pd(II) plane, respectively, as determined in X-ray crystal structures. It is evident that the differences in CCS values for 2+ species are not significantly large, and are presumably masked by the flexible N-hexyl chains of the ligand and subtle structural difference of **1·X** (e.g. Pd···Pd distance).

*5.3.7. Ion-Mobility spectrum of $(Pd_2L_4)(NTf_2)_4$ (**1/1'**).*

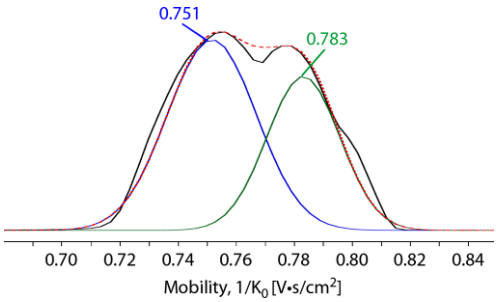

Figure S69. Extracted ion mobilogram of $[Pd_2L_4]^{4+}$ at *m/z* 606.7. A manual peak separation for two major components was carried out by curve fitting the spectrum using the Fityk software (M. Wojdyr, *J. Appl. Cryst.* **2010**, 43, 1126-1128). Shown are the experimental ion-mobility spectrum (black), simulated peak 1 (blue), simulated peak 2 (green), and sum of simulated peaks (red dash).

Table S5.2: Experimental and theoretical collision cross sections of $[Pd_2\mathbf{L}_4](NTf_2)_4$.[a]

Anion	*$[Pd_2\mathbf{L}_4]^{4+}$*					
	Mobility ($1/K_0$)	CCS (exp) (Å^2)	$CCS_{helical}$ (calcd) (Å^2)[b]	$CCS_{helical}$ (calcd) (Å^2)[c]	$CCS_{elongated}$ (calcd) (Å^2)[d]	$CCS_{elongated}$ (calcd) (Å^2)[e]
NTf^-	0.751(36)	605(29)	568.6(48)	606.9(36)	578.9(37)	643.1(53)
	0.783(33)	631(27)				

[a] Measured at 305 K in N_2 drift gas. [b, c, d, e] Obtained from the X-ray crystal structure of (b, c) **1·OTf** and (d, e) **1·NO_3** deduced computationally using the trajectory (TJ) method of the N2_MOBCAL program (b, d) without and (c, e) with partial charges on each atom. The partial charges were obtained single-point calculations with DFT method using B3LYP function. LanL2DZ and 6-31G(d,p) were employed to treat Pd and other atoms, respectively. The numbers in parentheses are the corresponding standard deviations.

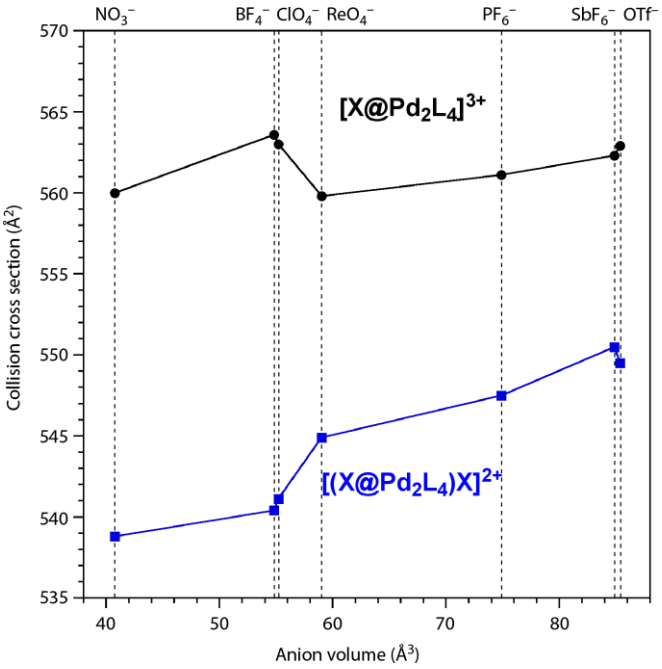

Figure S70. A graph showing the relationship between the anion volume and the collision cross sections (CCS) of $[X@Pd_2\mathbf{L}_4]^{3+}$ and $[(X@Pd_2\mathbf{L}_4)X]^{2+}$.

6. Electronic Structure Calculations

The host and combined host-guest geometries were optimized with RI-BP86,[16,17] the def2-SVP[18,19] orbital basis and the corresponding J-basis[20] using the TURBOMOLE package.[21] For the Pd atoms the ECP-28MWB pseudopotential[22] was used. The host and host-guest structures were taken from X-ray crystallography results. To lower the number of atoms and make the systems computationally more feasible the outer hexyl-groups were removed and carbazole nitrogens capped with methyl-groups. For the obtained minimum structures single point DF[23]-SCS[24]-LMP2[25,26] calculations were performed. The Dunning cc-pVTZ[27] orbital basis set was used in combination with the cc-pVTZ-PP[28] basis and the ECP28MDF[29] pseudopotential for Pd as well as the ECP60MDF[29] for Re (this basis will be referred to as VTZ). The density fitting basis used were the corresponding defaults (for the cc-pVTZ[30,31]) except for calculations with Pd and Re, where the JKFIT and MP2FIT def2-TZVPP[32,33] basis sets were used. The orbitals were localized by the Pipek-Mezey scheme.[34] The corresponding orbital domains were determined with a Boughton-Pulay criterion[35] at a threshold of 0.985. To speed up the calculations we made use of the multipole-approximiation[36] for very-distant pairs (r=10 Bohr) and local fitting.[23] All calculations were carried out with a development version of Molpro2018.1.[37] According to the locality of the orbitals we were able to build fragments (guest plus host) to determine the dispersion contributions[38,39] at the SCS-LMP2/VTZ level of theory, stabilizing the guest molecules.[40,41]

Table S5.3: Calculated structural parameters of **1·X** and corresponding dispersion contributions.

	Solid-state		Gas-phase	
Sample	**Pd···Pd distance (Å)**	**ΔEdisp kcal/mol**	**Pd···Pd distance (Å)**	**ΔEdisp kcal/mol**
1·BF_4	9.287	-10.77	7.911	-12.19
1·ClO_4	9.040	-19.52	7.902	-24.07
1·ReO_4	8.990	-31.35	8.038	-37.06
1·PF_6	8.713	---	8.066	---
1·SbF_6	8.805	---	8.280	---
1·OTf	9.400	---	8.880	---

Note: The values for dispersion in the case of PF_6, SbF_6 and OTf were not included due to difficulties in separating the orbital fragments.

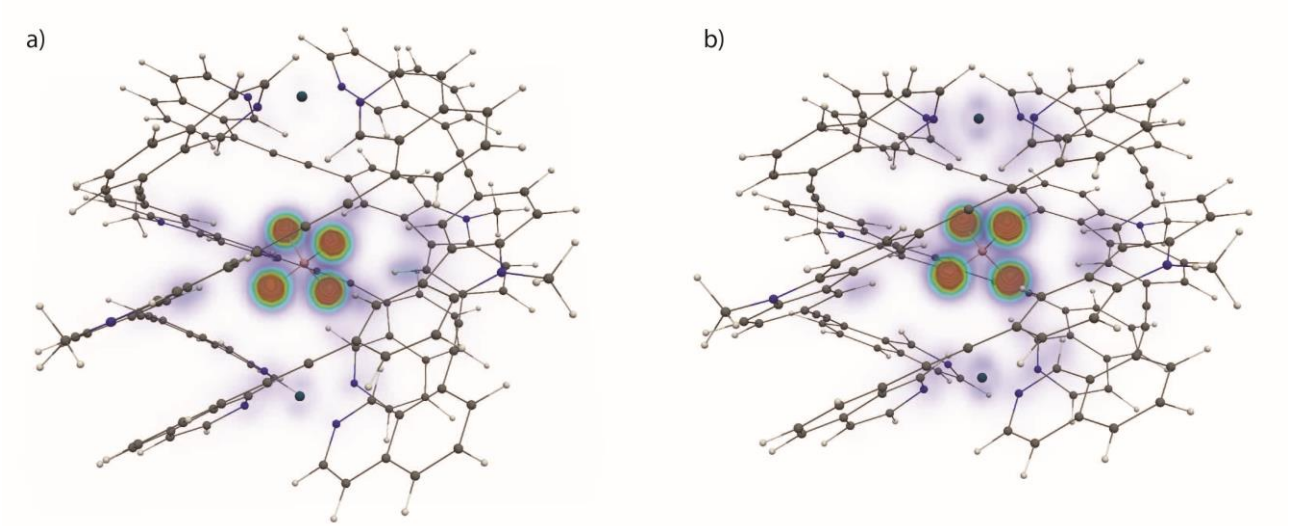

Figure S71. A VOXEL-DID structural representation of a) **1·BF_4** gas-phase structure (b) **1·BF_4** solid-state structure.

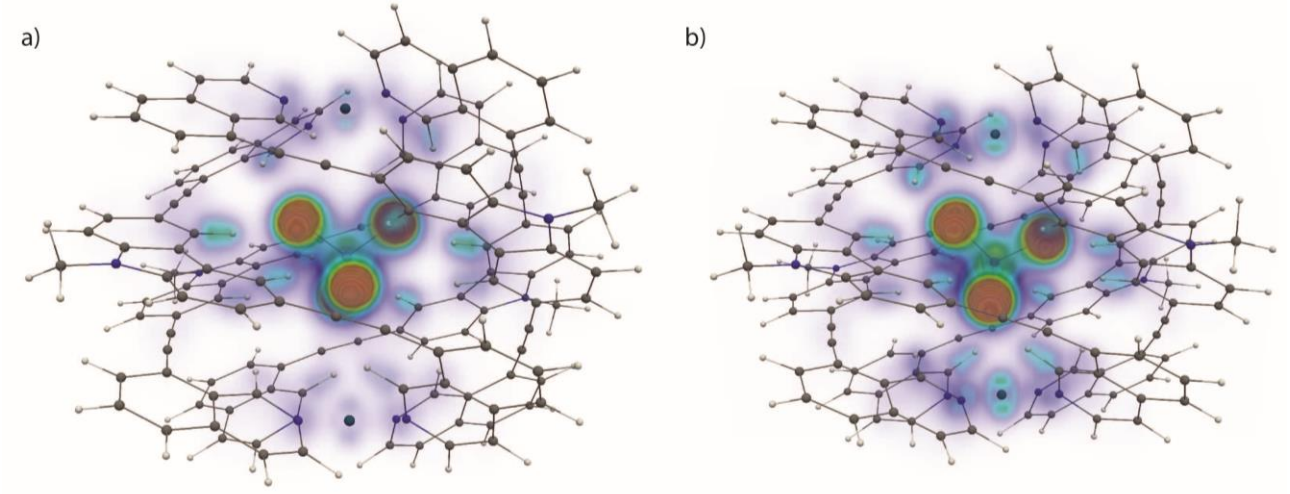

Figure S72. A VOXEL-DID structural representation of a) **1·ReO_4** gas-phase structure (b) **1·ReO_4** solid-state structure.

In order to investigate the experimental differences between gas-phase and solid-state, the host-guest systems were first optimized in a set of calculations with fixed Pd-Pd distances. This was followed by another series of completely relaxed structures. The DFT geometries achieved by the latter show a systematic shortening of the Pd-Pd distance. Thereby, the results reflect the calculated CCS-values for the host-guest systems, whereby guests with the same volume tend to form the same host geometry.

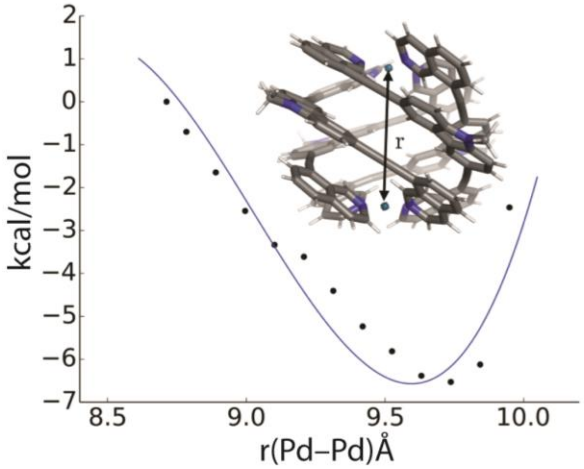

Figure S73. Results of a surface scan along the Pd-Pd axis performed for the empty cage. Thereby, the X-Ray host-structure of 1·PF6 served as the starting guess and the Pd-Pd distance was gradually increased by 0.2 Bohr and optimized. The resulting structures were recalculated at the DF-SCS-LMP2/VTZ level of theory. The revealed SCS-LMP2 minimum has a Pd-Pd distance of 9.7 Å, a larger value than all measured host-guest complexes, implying that the binding of the anion leads to an increased folding.

7. References

(1) Bag, P. P.; Wang, D.; Chen, Z.; Cao, R. *Chem. Commun.* **2016**, *52* (18), 3669.

(2) Li, Q.; Zou, J.; Chen, J.; Liu, Z.; Qin, J.; Li, Z.; Cao, Y. *J. Phys. Chem. B* **2009**, *113* (17), 5816.

(3) Bloch, W. M.; Abe, Y.; Holstein, J. J.; Wandtke, C. M.; Dittrich, B.; Clever, G. H. *J. Am. Chem. Soc.* **2016**, *138* (41), 13750.

(4) Neise, C.; Rautenberg, C.; Bentrup, U.; Beck, M.; Ahrenberg, M.; Schick, C.; Keßler, O.; Kragl, U. *RSC Adv.* **2016**, *6* (54), 48462.

(5) Burkhardt, A.; Pakendorf, T.; Reime, B.; Meyer, J.; Fischer, P.; Stübe, N.; Panneerselvam, S.; Lorbeer, O.; Stachnik, K.; Warmer, M.; Rödig, P.; Göries, D.; Meents, A. *Eur. Phys. J. Plus* **2016**, *131* (3), 56.

(6) Sheldrick, G. M. *Acta Crystallogr. Sect. A* **2015**, *71*, 3.

(7) Sheldrick, G. M. *Acta Crystallogr. Sect. C* **2015**, *71*, 3.

(8) Hubschle, C. B.; Sheldrick, G. M.; Dittrich, B. *J. Appl. Crystallogr.* **2011**, *44* (6), 1281.

(9) Kratzert, D.; Holstein, J. J.; Krossing, I. *J. Appl. Crystallogr.* **2015**, *48* (3), 933.

(10) Thorn, A.; Dittrich, B.; Sheldrick, G. M. *Acta Crystallogr. Sect. A* **2012**, *68* (4), 448.

(11) Spek, A. *Acta Crystallogr. Sect. C* **2015**, *71* (1), 9.

(12) Spek, A. *Acta Crystallogr. Sect. D* **2009**, *65* (2), 148.

(13) Fernandez-Lima, F. A.; Kaplan, D. A.; Park, M. A. *Rev. Sci. Instrum.* **2011**, *82*, 126106.

(14) Hernandez, D. R.; DeBord, J. D.; Ridgeway, M. E.; Kaplan, D. A.; Park, M. A.; Fernandez-Lima, F. *Analyst*, **2014**, *139*, 1913.

(15) Greisch, J.-F.; Chmela, J.; Harding, M. E.; Wunderlich, D.; Schäfer, B.; Ruben, M.; Klopper, W.; Schooss, D.; Kappes, M. M. *Phys. Chem. Chem. Phys*. **2017**, *19*, 6105.

(16) A. D. Becke, *Phys. Rev. A,* 1998, **38.6**, 3098.

(17) J. P. Perdew, *Phys. Rev. B,* 1986, **33.12**, 8822.

(18) K. Eichkorn, F. Weigend, O. Treutler, R. Ahlrichs; Theor. Chem. Acc., 1997, **97**, 119.

(19) F. Weigend, R. Ahlrichs; *Phys. Chem. Chem. Phys.*, 2005, **7**, 3297.

(20) F. Weigend, *Phys. Chem. Chem. Phys.*, 2006, **8**, 1057.

(21) TURBOMOLE V7.0 2015, a development of University of Karlsruhe and Forschungszentrum Karlsruhe GmbH, 1989-2015, TURBOMOLE GmbH, since 2007; available from http://www.turbomole.com.

(22) D. Andrae, U. Haeussermann, M. Dolg, H. Stoll, H. Preuss, *Theor. Chim. Acta*, 1990, **77**, 123.

(23) H.-J. Werner, F. R. Manby, and P. J. Knowles, *J. Chem. Phys.*,2003, **118**, 8149.

(24) S. Grimme, *J. Chem. Phys.*, 2003, **118.20**, 9095-9102.

(25) M. Schütz, G. Hetzer and H.-J. Werner, *J. Chem. Phys.*, 1999, **111**, 5691.

(26) G. Hetzer, M. Schütz, H. Stoll, and H.-J. Werner, *J. Chem. Phys.*, 2000, **113**, 9443.

(27) T. H. Dunning, *J. Chem. Phys.,* 1989, **90.2**, 1007-1023.

(28) K.A. Peterson, D. Figgen, M. Dolg, H. Stoll, *J. Chem. Phys.*, 2007, **126**, 124101.

(29) D. Figgen, K.A. Peterson, M. Dolg, H. Stoll, *J. Chem. Phys.,* **2009**, 130, 164108

(30) F. Weigend, A. Köhn and C. Hättig, *J. Chem. Phys.*, 2002, **116.8**, 3175-3183.

(31) F. Weigend, *J. Comput. Chem.*, 2008, **29.2**, 167-175.

(32) R. Gulde, P. Pollak & F. Weigend, *J. Chem. Theory Comput.*, 2012, ***8*(11)**, 4062-4068.

(33) C. Hättig, *Phys. Chem. Chem. Phys.*, 2005, ***7*(1)**, 59-66.

(34) J. Pipek and P. G. Mezey, *J. Chem. Phys.*, 1989, **90.9**, 4916-4926.

(35) J. W. Boughton, P. Pulay, *J. Comput. Chem.*, 1993, **14**, 736–740.

(36) G. Hetzer, P. Pulay, H.-J. Werner*, Chem. Phys. Lett.*, 1998, **290**, 143.

(37) H.-J. Werner, P. J. Knowles, R. Lindh, F. R. Manby and M. Schütz, *et al.*, *MOLPRO, version 2018.1, a package of ab initio programs*, 2017, see http://www.molpro.net

(38) M. Schütz, G. Rauhut, H. J. Werner, *J. Phys. Chem. A*, **1998**, *102(29)*, 5997-6003

(39) S. Grimme, J. Anthony, S. Ehrlich, H. Krieg, *J. Chem. Phys.* **2010**, 132, 15104

(40) A. Tkatchenko, D. Alfè, and K. S. Kim, *J. Chem. Theory Comput.* **2012**, 8.11, 4317-4322.

(41) P. Mikulskis, D. Cioloboc, M. Andrejić, S. Khare, J. Brorsson, S. Genheden, R. A. Mata & U. Ryde, *J. Comput. Aided Mol. Des.*, **2014**, *28*(4), 375-400.